Author Manuscript

Author Manuscript

Author Manuscript

Author Manuscript

HHS Public Access

Author manuscript

Nat Med. Author manuscript; available in PMC 2025 September 22.

Published in final edited form as:

Nat Med. 2019 April ; 25(4): 641–655. doi:10.1038/s41591-019-0379-5.

Platelet GPIbα is a mediator and potential interventional target for NASH and subsequent liver cancer

A full list of authors and affiliations appears at the end of the article.

Abstract

Non-alcoholic fatty liver disease ranges from steatosis to non-alcoholic steatohepatitis (NASH), potentially progressing to cirrhosis and hepatocellular carcinoma (HCC). Here, we show that platelet number, platelet activation and platelet aggregation are increased in NASH but not in steatosis or insulin resistance. Antiplatelet therapy (APT; aspirin/clopidogrel, ticagrelor) but not nonsteroidal anti-inflammatory drug (NSAID) treatment with sulindac prevented NASH and subsequent HCC development. Intravital microscopy showed that liver colonization by platelets depended primarily on Kupffer cells at early and late stages of NASH, involving hyaluronan-CD44 binding. APT reduced intrahepatic platelet accumulation and the frequency of platelet-immune cell interaction, thereby limiting hepatic immune cell trafficking. Consequently, intrahepatic cytokine and chemokine release, macrovesicular steatosis and liver damage were attenuated. Platelet cargo, platelet adhesion and platelet activation but not platelet aggregation were identified as pivotal for NASH and subsequent hepatocarcinogenesis. In particular, platelet-derived GPIbα proved critical for development of NASH and subsequent HCC, independent of its reported cognate ligands vWF, P-selectin or Mac-1, offering a potential target against NASH.

Reprints and permissions information is available at www.nature.com/reprints.

[*]**Correspondence and requests for materials** should be addressed to A.W. or M.H., achim.weber@usz.ch; heikenwaelder@helmholtz-muenchen.de.

Author contributions

M. Malehmir, D.P., S.G., M.S. and D.I. contributed equally as first authors. E.K., V.L., M.P. and B.G.J.S. contributed equally as second authors. Design of the study: M. Malehmir, M.J.W., D.R., A.W., B.N., M.G. and M. Heikenwaelder. M. Malehmir, E.K., D.P., V.L., M.J.W. and C.D. performed breeding and housing of mice. M. Malehmir, S.G., M.S., E.K., D.P., V.L., D.I., A.A., M.P., B.G.J.S., A.O., C.D., J.V., D.S., D.D., C.L.W., P.H., A.R., A.T., H.D., O.K., M.K., C.J.W., A.C., R.B., N.A., M.E.H., L.S. and M. Hinterleitner performed experiments. D.R., M.R., F.B., T.G., M.N.B., O.B., M.N. and M.G. designed and performed the clinical case study. J.W., R.P., N.D., L.Z., D.J.W, H.G.A, H.D., D.K., F.T., P.F.L., T.O., D.J.W., A.V., M.D.M., A.J.R., R.R., P.K., P.A.K., B.N., A.W., J.M.L, M. Matter, D.A.M., T.S., M.P., L.S., D.H.A., C.N.-A. and J.L. provided tissue samples or mouse strains and/or scientific input. K.U. and T.E. performed biostatistical analyses. All authors analyzed data. M. Malehmir, M.E.H., D.P., S.G., M.S., P.K., B.N., M.G., O.K., T.O., A.W., and M. Heikenwaelder wrote the manuscript, and all authors contributed to writing and provided feedback.

Online content

Any methods, additional references, Nature Research reporting summaries, source data, statements of data availability and associated accession codes are available at https://doi.org/10.1038/s41591-019-0379-5.

Competing interests

J.M.L. receives consulting fees from Bayer HealthCare Pharmaceuticals, Eli Lilly, Bristol-Myers Squibb, Merck, Eisai Inc, Celsion Corporation, Exelixis, Merck, Ipsen, Glycotest, Navigant, Leerink Swann LLC, Midatech Ltd, Fortress Biotech, Sprink Pharmaceuticals and Nucleix and research support from Bayer HealthCare Pharmaceuticals, Eisai Inc, Bristol-Myers Squibb and Ipsen. This article presents independent research supported in part by the National Institute for Health Research (NIHR) Birmingham Biomedical Research Centre. The views expressed are those of the author(s) and not necessarily those of the National Health Service, the NIHR, or the Department of Health.

Additional information

Extended data is available for this paper at https://doi.org/10.1038/s41591-019-0379-5.

Author Manuscript Author Manuscript Author Manuscript Author Manuscript

Non-alcoholic fatty liver disease (NAFLD) is the most common chronic liver disease in high-income countries[1] and is on trajectory to become the most common indication for liver transplantation in the United States[2,3]. NAFLD ranges from simple steatosis (non-alcoholic fatty liver (NAFL)) to NASH, which may progress to cirrhosis and ultimately to HCC[4,5]. HCC is the third most common cause of cancer-related death worldwide and is the fastest rising cancer in the United States and Europe[6–8]. Major risk factors for NASH include metabolic syndrome, abdominal obesity, insulin resistance, glucose intolerance or type 2 diabetes mellitus and dyslipidemia[4,5,9,10].

We previously developed a preclinical model of human metabolic syndrome, NASH and NASH-induced HCC[11]. In this model, intrahepatic influx of metabolically activated $CD8^+$ T cells and natural killer T (NKT) cells triggers metabolic reprogramming of hepatocytes, NASH and HCC development through cytokine-mediated cross-talk with hepatocytes. However, the mechanisms underlying immune cell recruitment during NASH and its consequences for NASH-to-HCC transition have remained unclear.

Platelets, produced by megakaryocytes in the bone marrow, play a fundamental role in hemostasis[12] but are also crucial in pathophysiological conditions like thrombosis, obesity, atherosclerosis, metastasis and stroke[13–15]. Additionally, a growing body of evidence highlights platelets as active players in liver disease and inflammation[13,16,17]. Notably, it has been reported that activated platelets contribute to cytotoxic T lymphocyte (CTL)-mediated liver damage in a model of viral hepatitis[18,19]. Moreover, blocking platelet activation and aggregation by aspirin-clopidogrel (Asp-Clo) abrogates hepatic T cell influx, subsequent liver damage and tumorigenesis without affecting peripheral T cell function in viral hepatitis[19,20]. Additionally, in a recent study of NAFL (but not NASH) patients, APT lowered serum markers of obesity and liver damage[21].

There is an unmet need for efficacious, low-risk therapies against NASH and NASH-to-HCC transition. Although several drugs (e.g., those decreasing blood sugar levels) are in phase 2 and 3 development[22,23], currently no approved pharmacological therapies are available that can prevent NASH or related pathologies. Further, the role of platelets in NASH and HCC development is not well characterized. Thus, we investigated whether APT and molecules involved in platelet function might prevent NASH and NASH-induced HCC development.

Results

Hepatic accumulation of activated platelets in NASH.

To test whether platelets contribute to NASH development, we investigated platelet number and distribution in livers of C57Bl/6 mice fed a choline-deficient, high-fat diet (CD-HFD). Platelet numbers (Fig. 1a) and aggregate size (Fig. 1b) were significantly increased compared with those of age-matched normal chow diet (ND)-fed controls (Fig. 1a), whereas platelet counts in peripheral blood remained normal (Supplementary Fig. 1a). Although fibrinogen levels and prothrombin time (PT) remained unchanged, activated partial thromboplastin time (aPTT) was significantly reduced (Supplementary Fig. 1a). Ex vivo analyses of circulating platelets revealed no significant differences in activation or aggregation responses in CD-HFD-fed mice compared with ND-fed mice (Supplementary

Author Manuscript Author Manuscript Author Manuscript Author Manuscript

Fig. 1b). We next analyzed other dietary and genetic murine NASH models (Fig. 1c–e and Supplementary Fig. 1c,d), including high-fat, high-fructose, high-cholesterol, 'Western-style' diets[24,25] with or without trans fat (WD-HTF; WD-NTF); a 'Western-style' diet with fructose (WD-FSDW)[26]; a methionine- and choline-deficient diet (MCD) and an inducible knock-in mouse expressing the human unconventional prefoldin RPB5 interactor (URI) in hepatocytes (hURI-tetOFFhep)[27]. All models induced NASH with varying NAFLD Activity Score (NAS) and degrees of fibrosis (Supplementary Fig. 2a,b), a primary determinant of outcome in NASH[28,29], and displayed a significant increase in intrahepatic platelet numbers compared to controls (Fig. 1a,c–e; Supplementary Fig. 1c,d). Further, human NAFLD/NASH patients displayed a significant increase in intrahepatic platelets in liver compared to healthy controls (Fig. 1f; Supplementary Table 1).

In contrast, mice fed a 45% kcal high-fat diet (HFD), displaying only steatosis, or mice fed a 60% kcal HFD with low sucrose (HFD-60% + LS) experiencing only simple steatosis and insulin resistance[30], lacked any significant increase in intrahepatic platelet numbers, despite increased body weight, NAS, liver damage and insulin resistance (Fig. 1g,h and Supplementary Fig. 3a–c). Intrahepatic platelet activation in NASH was confirmed by electron microscopy (EM) (Supplementary Fig. 3d). Thus, increased intrahepatic platelet number, platelet aggregation and platelet activation were specific to NASH.

Asp-Clo treatment is an APT currently used in several diseases (e.g., coronary stent thrombosis)[31]. We first addressed whether CD-HFD-fed mice would respond to APT. Compared with untreated CD-HFD-fed mice, Asp-Clo-treated mice displayed significantly lower intrahepatic platelet numbers (Supplementary Fig. 4a–c), as well as reduced platelet aggregation and activation (Supplementary Fig. 4d). To investigate the effects of APT on human NAFLD, we performed a pilot case study (German Clinical Trials Register (DRKS) 587/2016BO2) with patients at risk for NAFLD (body mass index >30 and/or diabetes mellitus type II) undergoing a heart catheter procedure. Depending on the outcome of the catheter procedure, one of three approaches was carried out: (1) patients received dual antiplatelet therapy (DAPT) for at least 6 months if a coronary stent was implanted; (2) ASA monotherapy was given for at least 6 months if coronary artery disease (CAD) was present but stent implantation was not indicated; (3) no anti-aggregation therapy was given if coronary artery disease was absent. None of the patients included received long-term treatment with ASA or P2Y12 before study inclusion (Supplementary Fig. 5a and Supplementary Table 2). In this pilot case study of 24 individual patients/observations, platelet function analyses revealed that patients generally responded well to APT (Supplementary Fig. 5b), although serum total cholesterol, LDL and HDL cholesterol remained unchanged (Supplementary Fig. 5b,c). For control, we investigated patients without APT (Supplementary Table 2). Patients with NAFLD underwent liver MRI, liver ultrasound and serum analysis at study inclusion and after 6 months of follow-up. APT-treated patients with NAFLD showed significantly reduced liver volume and liver fat mass (Supplementary Fig. 5d–f). Patients who received a new therapy with ASA or DAPT were diagnosed with CAD. The standard treatment in patients with CAD includes statins. Therefore, patients who received a new anti-aggregation therapy were usually treated with a new statin treatment if statins were not already administered on a regular basis and if contraindications were absent. Thus, statins might present a significant confounder in the

Author Manuscript Author Manuscript Author Manuscript Author Manuscript

actual pilot case study, which we tried to address by performing a linear regression analysis. Because the study collective was small, we included age, gender, anti-aggregation and new statin treatment in the regression analysis. For the course of liver fat, we found the strongest associations for anti-aggregation (b = −0.334, 95% CI −4.719, 1.197, P = 0.226), whereas initiation of a new statin treatment showed weaker associations (b = −0.095, 95% CI −3.551, 2.526, P = 0.726). For the course of liver volume, we found associations for anti-aggregation (b = −0,454, 95% CI –0.170, 0.006, P = 0.066) that were stronger compared with initiation of a new statin treatment (b = 0.047, 95% CI –0.084, 0.101, P = 0.847). This finding indicated that effects of anti-aggregation were stronger than those of statin administration. Notably, n = 4 patients showed significant reductions in liver fat content and/or liver volume without new statin therapy. However, there was a trend toward effect of anti-aggregation without being statistically significant. Higher body mass index did not significantly affect liver fat or liver volume.

Asp-Clo treatment attenuates NASH and NASH-associated conditions.

We next investigated whether Asp-Clo (adjusted to the body weight) affects NASH or HCC development in mice receiving ND, CD-HFD or CD-HFD with Asp-Clo for 12 months. Weight gain over time was significantly higher in CD-HFD and CD-HFD/Asp-Clo-fed mice compared with ND-fed controls (Fig. 2a). Similar to body weight, epididymal fat (eWAT) weight in CD-HFD/Asp-Clo-fed mice was not different from that in CD-HFD-fed mice (Supplementary Fig. 6a). Low platelet numbers were found in eWAT and remained unaltered (Supplementary Fig. 6b). $CD3^+$ T cell infiltration was significantly reduced by Asp-Clo (Supplementary Fig. 6c). RNA-seq analysis of eWAT from ND- and CD-HFD-fed mice revealed a different gene expression pattern resulting in spatial separation in the principal component analysis plot. Analysis of the most differentially expressed genes between diets showed upregulation of pathways involved in immune signaling, cell-cell interactions and extracellular matrix regulation in eWAT from CD-HFD-fed mice. In contrast, eWAT of CD-HFD-fed mice showed a significant downregulation in pathways involved in metabolism and antioxidant response (Supplementary Fig. 6d). ALT, AST, liver/body weight ratio, platelet numbers and aggregation state were significantly lower in livers of mice fed CD-HFD/Asp-Clo for 6 and 12 months (Fig. 2b, Supplementary Fig. 4a–d, Supplementary Fig. 7a,b). Asp-Clo significantly improved glucose tolerance (Fig. 2c), reduced liver triglycerides (Fig. 2d) and attenuated serum total cholesterol, LDL and HDL cholesterol (Fig. 2e and Supplementary Fig. 7c,d). Several genes involved in fatty acid β-oxidation, lipolysis and cholesterol metabolism are dysregulated during NASH development[11]. Asp-Clo treatment prevented downregulation of genes from all three groups (Fig. 2f). CD-HFD/Asp-Clo-fed mice lacked statistically significant changes in oxygen consumption, respiratory exchange ratio (RER), physical activity or in food and water intake compared with CD-HFD-fed mice (Fig. 2g,h and Supplementary Fig. 7e). These data were corroborated in WD-HTF-fed mice (Supplementary Fig. 7f,g).

To analyze platelet activation, P-selectin, a marker of α-granule release, and integrin αIIbβ3 activation were analyzed by means of flow cytometry. In Asp-Clo-treated CD-HFD-fed mice, circulating platelets showed markedly reduced integrin αIIbβ3 activation and P-selectin exposure compared with platelets in ND-fed and CD-HFD-fed mice in response

Author Manuscript Author Manuscript Author Manuscript Author Manuscript

to all tested agonists (Supplementary Fig. 8a), suggesting that Asp-Clo treatment effectively reduced platelet activation. Levels of major platelet surface glycoproteins were unchanged (Supplementary Fig. 8b).

MRI analysis revealed subcutaneous/abdominal fat accumulation in CD-HFD-fed and CD-HFD/Asp-Clo-treated mice, but not in ND-fed controls (Fig. 2i). However, liver steatosis was strongly ameliorated by Asp-Clo treatment in CD-HFD-fed mice (Fig. 2i). In contrast, untreated CD-HFD-fed mice displayed histopathological features of NASH, including liver fat deposition (Sudan red^{+} areas), fibrosis, damaged hepatocytes and lobular inflammation, including satellitosis (Figs. 2j,k and Supplementary Fig. 8c,d). We concluded that Asp-Clo treatment effectively prevented NASH development.

Asp-Clo treatment abrogates intrahepatic immune cell infiltration and inhibits NASH-induced HCC.

In addition to hepatic infiltration of CD3^{+}CD8^{+} T cells, CD11b^{+} MHCII^{+} myeloid cells and Ly6G^{+} granulocytes are increased in CD-HFD-fed mice, similar to human patients with NASH[11]. Immune cell infiltration was reduced in 6-month CD-HFD/Asp-Clo-treated mice (Fig. 3a). Flow cytometry analysis showed strong reduction in total number, effector differentiation (CD8^{+}CD62L^{-}CD44^{+}CD69^{+}) and proportion of CD4^{+}/CD8^{+} and NKT cells (Fig. 3b,c). B cells remained unchanged in 6-month ND-, CD-HFD- or CD-HFD/Asp-Clo-fed mice (Supplementary Fig. 9a,b).

Analyses of several potentially carcinogenic inflammatory signaling pathways activated under CD-HFD were dampened by Asp-Clo (Fig. 3d and Supplementary Fig. 9c). Asp-Clo significantly reduced CD11b+F4/80^{hi} Kupffer cells in livers of WD-HTF-fed mice (Supplementary Fig. 10a–d). An unbiased *t*-distributed stochastic neighbor embedding (t-SNE)-based clustering approach identified nine myeloid sub-clusters (Supplementary Fig. 11a,b and Supplementary Table 3). Asp-Clo significantly reduced the abundance of cluster 6, characterized by a high expression of CD11b, F4/80 and Gr1, closely resembling CD11b^{+}F4/80^{+} monocyte-derived macrophages (MoMFs). Further, a multiplex gene expression analysis for FACS-isolated Ly6C^{+} MoMFs, Ly6C^{-} MoMFs and Kupffer cells was performed. Principal component analysis of 561 genes revealed similar Ly6C^{+} MoMFs and Ly6C^{-} MoMFs in NASH-diet-fed mice with and without Asp/Clo treatment. However, Kupffer cells from WD-HTF/Asp-Clo livers clustered more closely to ND Kupffer cells than those of WD-HTF-fed mice (Supplementary Fig. 11a–d). This finding indicates that Asp-Clo influences the Kupffer cell compartment. Taken together, these data suggest that Asp-Clo treatment attenuated Kupffer cell activation, alongside reduced inflammatory myeloid cell infiltration in the injured liver. Altogether, Asp-Clo prevented NASH, reduced intrahepatic immune cell influx and dampened pathways potentially supporting hepatocarcinogenesis[32].

Next, we studied the effects of Asp-Clo treatment on CD-HFD-induced HCC[11]. Thirteen of 51 CD-HFD livers (~25%) displayed macroscopically visible tumors by 12 months (Fig. 3e–g). In contrast, CD-HFD/Asp-Clo-treated mice lacked macro- and microscopically visible liver tumors (Fig. 3e–g and Supplementary Fig. 12a). CD-HFD-fed mice treated with a lower dose of Asp-Clo (according to the initial body weight and not further adjusted to

Author Manuscript Author Manuscript Author Manuscript Author Manuscript

diet or age-related weight gain) developed significantly fewer HCC (3/52) compared with untreated CD-HFD-fed mice (13/51) (Supplementary Fig. 12b). Therefore, continuously adjusting the dose of Asp-Clo to body weight is critical to fully prevent HCC.

Asp/Clo dampens hepatic cytokine expression, platelet–liver endothelium and platelet–immune cell interactions.

Gene expression and signaling pathway analyses of ND, CD-HFD and WD-HTF livers revealed a significant induction in gene expression profiles involved in platelet activation, aggregation and degranulation (Extended Data Fig. 1a–i). Moreover, NASH-related enrichment of genes was associated with expression of TNF superfamily members, cytokine and chemokine production and chemotaxis[11,27] (Extended Data Fig. 1a–i). Asp-Clo treatment significantly attenuated the latter, some of which are also released from activated platelets (e.g., CCL5, TGFβ)[33] (Supplementary Fig. 13a).

Coupling high-resolution confocal microscopy and 3D reconstruction of liver sinusoids enabled visualization and quantification of platelet interactions with the liver endothelium and immune cells. Asp-Clo reduced NASH-related increase of platelet interaction with the liver endothelium, T cells and innate immune cells (Supplementary Fig. 13b–f and 14a,b).

To exclude COX2-dependent effects of Asp-Clo, we used another NSAID/COX1/2 inhibitor, sulindac. CD-HFD/sulindac-treated mice exhibit obesity; no significant changes in liver/body weight ratio, hepatic triglycerides and glucose tolerance; no significant alteration in gene expression involved in metabolism; severe steatosis; and increased liver damage comparable to that of CD-HFD-fed mice (Extended Data Fig. 2a–f). Thus, Asp/Clo-mediated effects on NASH are COX independent.

To corroborate our results with another platelet inhibitor, CD-HFD-fed mice were treated with ticagrelor (CD-HFD/ticagrelor), an FDA-approved direct and reversible antagonist of the platelet P2Y12 receptor[34] for coronary artery disease used in the clinic (e.g., with ASA after coronary stent implantation in patients presenting with an acute coronary syndrome without increased bleeding risk)[35]. Intrahepatic platelet number, platelet/liver endothelium coverage, platelet aggregation, liver damage, liver triglycerides and serum cholesterol were significantly reduced in ticagrelor-treated mice, whereas very-low-density lipoprotein secretion was not affected (Extended Data Fig. 3a–h). Expression of genes involved in cholesterol metabolism, ‘de novo’ lipogenesis and lipid storage were unchanged by the treatment, whereas downregulation of several genes involved in fatty acid oxidation and lipolysis that occurs in CD-HFD-fed mice (Extended Data Fig. 3i,j) and in histopathological features of NASH were prevented by ticagrelor (Supplementary Fig. 15a–c). Total numbers, activation and proportion of $CD4^+/CD8^+$, $CD8^+CD62L^-$ $CD44^+CD69^+$ and $CD3^+NK1.1^+$ cells were also reduced (Supplementary Fig. 15d,e). In contrast to liver tissues, increased expression of genes involved in inflammation and fibrosis was found in eWAT from CD-HFD- and WD-HTF-fed mice receiving Asp-Clo or ticagrelor (Supplementary Fig. 15f). This finding indicates that APT is beneficial specifically to the liver, affecting intrahepatic platelets and immune cell infiltration and improving hepatic steatosis by maintaining normal expression of genes involved in lipid catabolism.

Author Manuscript Author Manuscript Author Manuscript Author Manuscript

We next investigated whether ticagrelor would affect NASH-to-HCC transition. Compared with that in untreated CD-HFD-fed mice, ticagrelor treatment significantly reduced HCC development. One tumor was detected in 29 livers of CD-HFD/ticagrelor-treated mice (Supplementary Fig. 16a). The therapeutic potential of ticagrelor was tested in CD-HFD-fed mice with fully established NASH (4-month CD-HFD), followed by 8 weeks of ticagrelor treatment with CD-HFD. Intrahepatic platelet numbers, NAS and liver damage were reduced, but no difference in glucose tolerance was found (Supplementary Fig. 17a,b), and no effect on the blood immune cell populations was observed (Supplementary Fig. 17c). Similar results were obtained with therapeutic ticagrelor treatment in the context of a WD-HTF and of fibrosis; no difference in whole-body metabolism was found upon ticagrelor treatment in CD-HFD or WD-HTF mice (Supplementary Figs. 17d,e and 18a,b).

Early platelet recruitment in fatty liver correlates with liver damage, hepatocyte swelling and reduced sinusoidal diameter.

To understand the dynamics of intrahepatic platelet recruitment and attachment during the initial events of NAFL preceding NASH, we performed intravital microscopy in CD-HFD or WD-HTF-fed mice over 4, 5, 6 and 8 weeks post diet induction (Fig. 4a and Supplementary Fig. 19a–c). Platelets were the first non-resident cell type to populate the liver at ≤4 weeks post diet induction in both CD-HFD- and WD-HTF-fed mice (Fig. 4a–d and Supplementary Fig. 19a–c). Platelets progressively aggregated and increased in number in liver sinusoids over 8 weeks in the absence of significantly elevated $CD3^+$ T cells or $Ly6G^+$ granulocytes (Fig. 4a–d and Supplementary Fig. 19a–c). Even at this early stage, mild steatosis, reduced sinusoidal diameter and hepatocyte swelling were observed (Fig. 4e,f and Supplementary Fig. 19e). NAS and liver triglycerides were increased in CD-HFD- and WD-HTF-fed mice (Fig. 4g,h and Supplementary Fig. 19d–f). Platelets interacted primarily with Kupffer cells, as determined by 3D high-resolution reconstruction (Fig. 4i). Although intrahepatic granulocyte numbers remained unaltered in the first 8 weeks post diet induction, granulocytes might still support intrahepatic platelet recruitment and NAFL and NASH induction. Administration of anti-Ly6G antibodies via osmotic pumps for 8 weeks to CD-HFD-fed mice did not reduce intrahepatic platelet numbers but successfully reduced granulocytes. Experiments revealed no significant role of granulocytes in the early development of NAFL and borderline NASH (Supplementary Fig. 20a–e).

We next screened for possible adhesion molecules and danger markers responsible for early platelet attachment and recruitment. We found progressive induction of the extracellular matrix component hyaluronan colocalizing with hepatocytes, Kupffer cells and, to a lesser degree, on liver sinusoidal endothelial cells (LSECs) (Fig. 4j).

Kupffer cell-dependent platelet recruitment involving hyaluronan-CD44 binding supports early and advanced stages of NAFL including NASH.

To investigate the functional role of Kupffer cells and molecules involved in platelet–LSEC and platelet–immune cell interaction (e.g., hyaluronan, CD44) in borderline NASH, CD-HFD- or WD-HTF-fed mice were treated with clodronate liposomes (CLL), control liposomes (CL), hyaluronidase (HYAL), HYAL/CLL (double treatment), CD44-binding/HA-blocking AB (clone KM81) or CD44-binding/HA-non-blocking AB (clone

Author Manuscript Author Manuscript Author Manuscript Author Manuscript

IM7), for control (Fig. 5a and Supplementary Fig. 21a,b). Treatment with CLL and CLL/HYAL, but not CL reduced Kupffer cell numbers in CD-HFD- and WD-HTF-fed mice (Fig. 5b and Supplementary Fig. 21c,d). CLL and HYAL reduced NAS significantly in CD-HFD- and WD-HTF-fed mice (Fig. 5b and Supplementary Fig. 21d). CLL and HYAL treatments significantly reduced intrahepatic platelets (Fig. 5c); a significant reduction in liver damage was found following HYAL but not CLL (Fig. 5d). Combined treatment with both CLL and HYAL did not result in a further decrease of platelet numbers (Supplementary Fig. 21f,g). Similar data (platelet reduction and NAS reduction) with CLL treatment were obtained using WD-HTF-fed mice, although ALT levels remained elevated (Supplementary Fig. 21d,e). Also, treatment with a CD44-binding/HA-blocking, but not with a CD44-binding/HA non-blocking antibody led to a reduction in NAS and liver damage (Fig. 5e–g).

Notably, significantly reduced NAS, platelet accumulation, triglycerides, and liver damage by CLL treatment in mice fed CD-HFD for 6 months demonstrate a potential therapeutic effect of CLL even in a short treatment scheme (Fig. 5h,i and Supplementary Fig. 22). These data imply that Kupffer cells, hyaluronan and CD44 are important players in the early and advanced stages of NAFL, including NASH.

Platelet cargo is indispensable for NASH development.

Platelets release bioactive factors from intracellular granules in response to cellular activation. During thrombo-inflammatory reactions, the mostly proteinous components of α-granules are essential for immune cell recruitment and tissue damage[36]. Nbeal2-knockout mice (*Nbeal2*$^{-/-}$), which lack α-granules in platelets and are thus protected from thrombosis and thrombo-inflammatory tissue damage[37–39] were on a CD-HFD for 6 months. CD-HFD-fed *Nbeal2*$^{-/-}$ mice displayed no significant difference in intrahepatic platelet number or aggregation and gained weight similarly to CD-HFD-fed controls (Fig. 5j and Supplementary Fig. 23a). Still, significantly lower serum ALT and AST levels were found in CD-HFD-fed *Nbeal2*$^{-/-}$ mice compared with those in CD-HFD-fed mice (Fig. 5k). This finding was paralleled by a significant decrease in liver triglycerides, lower serum cholesterol (Fig. 5l,m), and improved glucose tolerance in CD-HFD-fed *Nbeal2*$^{-/-}$ mice (Supplementary Fig. 23b). Deregulation of lipid metabolism genes found in CD-HFD livers was partially prevented in CD-HFD-fed *Nbeal2*$^{-/-}$ mice (Supplementary Fig. 23c). CD-HFD *Nbeal2*$^{-/-}$ livers lacked steatosis and NASH and displayed a lower NAS (Fig. 5n and Supplementary Fig. 23d). Suppression of NASH in *Nbeal2*$^{-/-}$ mice on CD-HFD was corroborated by significant diminution of lipid content (Fig. 5o). Decreased T cell infiltration, neutrophil accumulation and macrophage activation were found in *Nbeal2*$^{-/-}$ mice on CD-HFD (Supplementary Fig. 23e). Together, these results indicated that platelet α-granule components contribute to NASH.

CD-HFD-induced NASH could not be rescued in mice lacking the GPIIb subunit of the platelet fibrinogen receptor GPIIb/IIIa (integrin α2β3; *Itga2b*$^{-/-}$ mice) which harbors activatable platelets unable to aggregate (Extended Data Fig. 4). This is in agreement with a recent study indicating that deletion of the platelet integrin α2β3 binding motif of fibrinogen did not alter NASH[40].

Author Manuscript Author Manuscript Author Manuscript Author Manuscript

Moreover, mice lacking the activating platelet collagen receptor glycoprotein VI (GPVI; *Gp6*$^{-/-}$)[41], the platelet-derived C-type lectin-like receptor 2 (*Clec-2*$^{-/-}$) or the hematopoietic cell–specific podoplanin (*Pdpn*$^{-/-}$) all developed NASH and NASH-associated conditions upon CD-HFD feeding (Extended Data Figs. 5–6).

Mucosal vascular addressin cell adhesion molecule 1 (MAdCAM-1) was recently discovered as an important player in NASH[42]. Animals with genetic depletion of MAdCAM-1 presented lower NAS and less liver damage after 6-month of WD-HTF[42]. We analyzed livers of WD-HTF-fed mice lacking MAdCAM-1 (*MAdCAM-1*$^{-/-}$), L-selectin (*L-sel*$^{-/-}$), integrin beta7 ($\beta7^{-/-}$) and both L-selectin and integrin beta7 (*L-sel*/$\beta7^{-/-}$). *MAdCAM-1*$^{-/-}$ mice displayed significantly reduced intrahepatic platelet numbers correlating with a partial protection from NASH (Extended Data Fig. 7a,b). In contrast, deletion of MAdCAM-1 ligands integrin beta7, L-selectin and L-selectin/integrin beta7 did not affect intrahepatic platelet numbers or platelet aggregation and did not prevent, or only partially prevented, NASH (Extended Data Fig. 7a, b).

Platelet GPIbα and α-granules are required to induce NASH.

Our data demonstrate that intrahepatic interaction of platelets with Kupffer cells, involving hyaluronan/CD44 binding and platelet cargo function, but not platelet aggregation contribute to NASH. Platelet-derived GPIbα has been implicated in platelet attachment and activation[43]

We thus hypothesized that GPIbα might mediate early platelet-trafficking/activation in NASH livers[43]. We first analyzed the interaction of GPIbα with parenchymal and non-parenchymal liver cells (LSECs; Kupffer cells, etc.) in NASH. 3D reconstruction revealed that the most abundant interactions of GPIbα^{+} platelets were with Kupffer cells and less so with LSECs in mouse and human NASH samples (Fig. 6a,b; Supplementary Fig. 24a).

Thus, we blocked the major ligand binding domain of GPIbα in 6-month CD-HFD-fed mice therapeutically using antigen-binding fragments (Fab) of the anti-GPIbα antibody pop/B[44] for 5 weeks. Notably, this short therapeutic treatment significantly reduced intrahepatic platelet accumulation in the presence of CD-HFD (Fig. 6c,d). Consequently, steatosis, NAS, liver damage, liver triglycerides and intrahepatic immune cell infiltration were reduced; fibrosis was dampened (Fig. 6c–h and Supplementary Fig. 24b–d). Additionally, anti-GPIbα antibody treatment reduced intrahepatic protein expression of several pro-inflammatory and homeostatic cytokines and chemokines, including CCL5, CCL6, ICAM-1, P-selectin and CD40, linking intrahepatic platelet activation and Nbeal2-dependent cargo release with mediators of inflammation (Supplementary Fig. 24e).

We next tested whether therapeutic anti-GPIbα antibody treatment would prevent fatty liver-to-NASH transition in early disease progression (e.g., after 6-week CD-HFD; Fig. 4). However, these treatments did not ameliorate NAFL/ borderline NASH, most likely due to lack or low expression of yet unidentified GPIbα ligands at early disease stages (Supplementary Fig. 24f,g). These data highlight distinct mechanisms of platelet recruitment in early versus established NAFL/borderline NASH—still involving Kupffer cells at both disease stages.

Author Manuscript Author Manuscript Author Manuscript Author Manuscript

To corroborate the above data in a genetic model, we fed transgenic mice expressing an IL-4rα/GPIbα fusion-protein in a *GPIbα*$^{-/-}$ background[45] in which the ligand-binding ectodomain of GPIbα is replaced by the α-subunit of the human IL-4 receptor (*hIL4rα/GPIbα*-Tg)[45] with a CD-HFD for 6 months. Remarkably, platelet aggregate size, platelet area and platelet–liver endothelium coverage were significantly lower in CD-HFD-fed *hIL4Rα/GPIbα*-Tg mice compared with those off CD-HFD-fed C57Bl/6 controls (Supplementary Fig. 25a–c). Both *hIL4rα/GPIbα*-Tg and C57Bl/6 mice gained weight similarly when fed a CD-HFD (Supplementary Fig. 25d). Serum cholesterol, liver triglycerides, serum ALT and AST levels were significantly lower in CD-HFD/*hIL4rα/GPIbα*-Tg mice (Fig. 6i,j; Supplementary Fig. 25e), accompanied by less LDL and HDL cholesterol (Supplementary Fig. 25e). Similarly, dysregulated mRNA expression of lipid metabolism-related genes in livers of CD-HFD-fed C57BL/6 mice was prevented in livers of CD-HFD/*hIL4rα/GPIbα*-Tg mice (Supplementary Fig. 25f). We also observed strong and significant reductions in intrahepatic CD8^{+} T and NKT cells by flow cytometry analysis (Fig. 6k). Reduced CD3^{+} and reduced macrophage influx and activation were observed using immunohistochemistry (Supplementary Fig. 25g,h). CD-HFD/*hIL4rα/GPIbα*-Tg mice showed lower intrahepatic protein expression of several pro-inflammatory and homeostatic cytokines and chemokines, including CCL5, CD40 and TNFRSF11B (Supplementary Fig. 25i), mechanistically linking platelet attachment and activation and cytokine and chemokine expression to efficient intrahepatic immune cell attraction. CD-HFD/*hIL4rα/GPIbα*-Tg mice lacked histological features of NASH, paralleled by a reduction in lipid accumulation and absence of macrovesicular steatosis analyzed by H&E and Sudan red staining (Fig. 6l–o).

Notably, mice lacking the major platelet adhesion receptors P-selectin (*Selp*$^{-/-}$)[46], von-Willebrand-factor (*vWF*$^{-/-}$)[47] or Mac-1 (*Mac-1*$^{-/-}$)[48], the known ligands of GPIbα, displayed full-blown NASH after 6 months of CD-HFD (Extended Data Figs. 8–10).

Finally, we investigated whether *hIL4rα/GPIbα*-Tg mice would develop HCC upon long-term CD-HFD. Of note, *hIL4rα/GPIbα*-Tg mice receiving CD-HFD for 12 months displayed significantly lower fibrosis and serum ALT, and lacked any macro- or microscopic evidence of HCC (Fig. 6p–u).

Discussion

It is becoming increasingly clear that beyond their central role in hemostasis and wound repair after vascular injury[49], platelets are key players in multiple pathophysiological conditions[16–18,20], including cytotoxic T lymphocyte–mediated liver damage and associated pathologies[18]. Here, we identified Kupffer cells as key players in intrahepatic platelet recruitment in early and advanced stages of NAFL, borderline NASH and NASH. In early NAFL and borderline NASH, hyaluronan and CD44 binding are also involved. In late NASH, GPIbα expressed by platelets appears to be primarily involved in the interaction of platelets with Kupffer cells and in the maintenance of NASH. Thus, Kupffer cells play distinct roles in intrahepatic platelet recruitment at different NAFLD stages.

Author Manuscript Author Manuscript Author Manuscript Author Manuscript

We found no evidence for a role of platelet-derived GPIIb/IIIa (*Itga2b*$^{-/-}$ mice) in NASH, suggesting that platelet activation and adhesion are important, whereas platelet aggregation is dispensable.

What is the function of platelets recruited to the liver? Our results indicate a major contribution of the platelet cargo function (α-granule components) in NASH progression, exemplified by the marked protection of *Nbeal2*$^{-/-}$ mice. The exact nature of platelet-derived α-granule constituents is currently unclear. However, several chemokines and cytokines were reduced upon therapeutic anti-GPIbα antibody treatment in the liver, suggesting that the number and activation state of intrahepatic platelets directly or indirectly correlate with an increase in immune cell–attracting chemokines and cytokines.

The key role of GPIbα in NASH identified in this study parallels a similarly vital function of this receptor in the development of experimental autoimmune encephalomyelitis (EAE), where it orchestrates the recruitment of leukocytes to the inflamed CNS[50]. Our results, similar to those of the EAE study, argue against a key role of the three known cognate interaction partners of GPIbα: P-selectin, vWF and Mac-1 (refs. [48,51,52]) and point to a GPIbα-activation-dependent proinflammatory function of α-granules in intrahepatic immune cell attraction.

Selectins have also been shown to be dispensable for leukocyte recruitment in inflamed liver microvasculature[53]. Other interaction partners might be involved (e.g., coagulation factors XI, XII). It is also conceivable that GPIbα exerts its function in disease development independent of an ectopic ligand[54]. Moreover, due to the complex pathogenesis underlying NASH, it is plausible that GPIbα is not the only molecule involved. Mice lacking MAdCAM-1 (*MAdCAM-1*$^{-/-}$) also showed significantly reduced intrahepatic platelet infiltration, but the exact mechanisms by which this occurs is unknown.

Cholesterol also plays a pivotal role during NASH pathogenesis by inducing hepatic lipotoxicity[55]. Notably, different Western diets (e.g., HTF and NTF) with high cholesterol recapitulated platelet-dependent phenotypes (increased intrahepatic platelets and responsiveness to therapeutic APT) described in the CD-HFD, but with a more pronounced NASH phenotype with higher NAS and fibrosis.

Of note, platelets and platelet-derived GPIbα are potential therapeutic targets of NASH and subsequent HCC development. Although GPIbα-antibody treatment induces prolonged bleeding time, it does not induce spontaneous bleeding[44], as only one GPIbα epitope is blocked, leaving receptor function largely intact. Thus, GPIbα antibody is a potentially safe new treatment modality against a metabolic disease of major public health burden[4,9]. So far, there is no drug treatment available specifically targeting NASH. The use of pioglitazone (most promising drug so far, off-label outside type II diabetes mellitus because of side effects) or vitamin E (better safety and tolerability in the short term) or combination thereof could be used for NASH treatment[4,56]. Other agents such as obeticholic acid have also improved histological features of NASH, although data with respect to their long-term benefits are still awaited[57]. Combined therapies for NASH treatment are currently being pursued, as only a subset of patients respond well to monotherapies[5]. This might be

Author Manuscript Author Manuscript Author Manuscript Author Manuscript

overcome by stratifying more responsive patients to a given monotherapy or by utilizing multitarget drugs. A viable approach might be a metabolic target in combination with an anti-inflammatory or anti-fibrotic drug, such as APT and statins, as described in our pilot case study. Nevertheless, given that APT and anti-GPIbα treatment attenuated metabolic dysfunction, inflammation and fibrosis, these modalities constitute potential monotherapies against NASH. Although a risk for bleeding cannot be excluded for both, which warrants careful monitoring, a single-substance therapy is expected to harbor a lower risk of side effects compared with combined therapies.

Given that only a proportion of patients with NAFLD progress to NASH and HCC, the question remains at which stage of NAFLD such treatments should be initiated. Future studies are needed not only to identify novel druggable targets for NASH and HCC, but also to identify non-invasive biomarkers for detection of early NAFLD and NASH, when it is still amenable to therapeutic intervention. It was recently demonstrated that higher serum ALT correlated with HCC development not only in a mouse model of chronic liver cell damage, but also in patients with chronic liver disease of diverse etiology including NASH[11,58].

Prophylactic APT, commonly used for acute and long-term treatment of coronary artery disease[59], and ticagrelor attenuate NASH and NASH-induced HCC[16]. In contrast, sulindac did not prevent NASH in mice. Thus, rather than NSAIDs in general, therapies that specifically block intrahepatic platelet accumulation or platelet function seem to be required to prevent NASH and NASH-associated conditions.

For NASH, we also observed a therapeutic effect of APT in preventing NASH-triggered HCC (although potential therapeutic effects of APT in the context of pre-existing HCC was not tested)[60]. Similarly, we have observed a therapeutic anti-NASH effect of anti-GPIbα antibody treatment. Remarkably, in both cases, therapeutic treatment partially dampened fibrosis.

Furthermore, in a small prospective human cohort study, APT reduced liver volume and liver fat accumulation in patients with NAFLD, thus supporting the results of our murine in vivo experiments. The results of this pilot case study, being a starting point for further studies, have to be interpreted with caution as it is currently underpowered. Although a multivariate analysis on a small patient cohort inherently warrants careful interpretation, our data have shown that effects of anti-aggregation were stronger than those of statin administration.

In our study, NASH prevention (e.g., by two distinct APTs, ticagrelor and Asp/Clo, in hIL4rα/GP1bα-Tg mice) ultimately suppressed subsequent HCC formation, mostly because the pro-carcinogenic NASH-related environment (e.g., intrahepatic inflammation, signaling, hepatocyte damage) was lacking. Moreover, treatment with anti-GPIbα antibody or depletion of Kupffer cells abrogated NASH therapeutically. These approaches might have an important impact for chemo-preventive strategies, which are still lacking in NASH treatment. Thus, our findings provide a rationale for APT, P2Y12 antagonists or reagents directly blocking platelet-derived GPIbα or related pathways as possible therapeutic approaches for patients with NASH, not only to prevent or revert NASH but also to prevent NASH-to-HCC transition.

Author Manuscript Author Manuscript Author Manuscript Author Manuscript

Methods

Mice, diets and treatments.

Mice 4 to 5 weeks old (C57BL/6 JOlaHsd) were purchased from ENVIGO. P-selectin knockout mice (*Selp*$^{-/-}$) and MAC-1 knockout mice were purchased from Jackson Laboratories (mouse strains 002289 and 003991). Knockout mice for *Nbeal2*$^{-/-}$, GPVI (*Gp6*$^{-/-}$)[61], GPIIb/IIIa (*GpIIb*$^{-/-}$; *Itga2b*$^{-/-}$), von Willebrand factor (*vWF*$^{-/-}$) and transgenic mice, lacking functional GPIbα, hIL4rα/GPIbα-Tg, all on the background of C57Bl/6J were kindly provided by B. Nieswandt and J. Ware (University Hospital and Rudolf Virchow Center, University of Würzburg, Würzburg, Germany; Department of Physiology and Biophysics, University of Arkansas for Medical Sciences, Little Rock, AR, USA). Tissues from inducible knock-in mice expressing the human unconventional prefoldin RPB5 interactor (URI) in hepatocytes (hURI-tetOFFhep) were received from N. Djouder, CNIO, Madrid. *Pdpn*$^{fl/fl}$ x Vav1-iCre mice (obtained from Jackson Laboratories) and *Clec1b*$^{fl/fl}$ x Pf4-Cre mice are described elsewhere[62]. All strains of genetically altered mice were on a C57BL/6J background. Control mice were negative for Cre recombinase and matched by genetic background, age and sex. Mice were housed at the University Hospital Zurich (USZ), the Technical University Munich/Helmholtz Zentrum Munich, the Biomedical Services Unit at University of Birmingham or University of Newcastle, the University of Calgary, RWTH Aachen University and the German Cancer Research Center (DKFZ). All animal work was conducted under the approval of the Swiss Veterinary Office (136/2014), according to German Law (G7/17, 55.2-1-54-2532-39-2015, G-91/14 and AZ:84-02.04.2014.A010), the UK Animals Scientific Procedures Act of 1986, with project license approval granted by the UK Home Office, the local biomedical research ethics committee approval, the Newcastle Ethical Review Committee under UK Home Office project license P3F79C606 and the University of Calgary Animal Care Committee (protocol AC16-0148) in accordance with the Canadian Council for Animal Care Guidelines. Animals were maintained under specific-pathogen-free conditions and experiments were performed in accordance with the guidelines of the respective institution and were in accordance with ethical regulations and humane endpoints.

Five-week-old mice were fed ad libitum: a normal diet (ND) (Provimi Kliba) or a choline-deficient high-fat diet (CD-HFD) (Research Diets; D05010402) for 6 or 12 months; a Western diet with trans-fat (WD-HTF) (Research Diets; D09100301: 40 kcal % fat (Primex shortening), 20 kcal % fructose, 2% cholesterol) for 6 or 7.5 months; or a methionine-choline-deficient diet (MCD) (MP Biomedicals) for 4 weeks; and control mice were fed a calorifically matched control diet, a Western diet with fructose in drinking water (WD-FSDW) (Custom Research Diet TD.06303; Harlan Laboratories in conjunction with fructose-supplemented drinking water: 55% fructose, 45% glucose by weight at a concentration of 42 g/l) ad libitum for 6 and 9 months. Control animals received ND and non-supplemented drinking water.

Cohorts of mice fed CD-HFD or WD-HTF were in addition treated with either aspirin (through food pellets containing 7.5 mg per kg of food) in combination with clopidrogel high (40 μg/ml drinking water; ~3 mg/kg/day) or low dose (20 μg/ml drinking water; ~1.5

Author Manuscript Author Manuscript Author Manuscript Author Manuscript

mg/kg/day), with sulindac (200 μg/ml drinking water; ~20 mg/kg/day) or with ticagrelor (40 μg/ml drinking water; ~3 mg/kg/day).

For interventional studies 5-week-old male mice were fed a normal diet (ND), a choline-deficient high-fat diet (CD-HFD) (Research Diets; D05010402) or a Western diet containing trans-fat (WD-HTF) (Research Diets, D09100301) for 3.5 weeks and then treatment started for 2.5 weeks, twice per week intravenously in 100 μl PBS of either 20 μg/mouse anti-CD44 antibody (clone KM81, Cedarlane, CL8944AP), 100 μg/mouse anti-CD44 (clone IM7, Bioxcell, BE0039), 100 μl/mouse Clodrosome (liposomal clodronate), 100 μl/mouse Encapsome (Control Liposomes), 100 μg/mouse anti-GPIbα or 100 μg/mouse Fab-Rat IgG (kindly provided by B.N., University Hospital and Rudolf Virchow Center, University of Würzburg, Würzburg, Germany) or intraperitoneally 20 U/g murine hyaluronidase (HYAL). In late treatment regimes, mice were fed CD-HFD for 6 months and treated with the same protocol for indicated time points.

For the osmotic pump experiment, 5-week-old male mice were fed a choline-deficient high-fat diet (CD-HFD) (Research Diets; D05010402) for 12 weeks. Four weeks after the diet, mini pumps (Alzet, model 2004) were implanted subcutaneously into the mice to deliver 30 μg per day of Ly6G (clone 1A8, Bioxcell, BP0075) neutrophil-depleting antibody or Rat IgG2a (clone 2A3, Bioxcell, BE0089) for 8 more weeks. At the end of the experiment, animals were culled, and the liver, fat and serum were harvested for analysis.

Human material.

Specimens were obtained from formalin-fixed, paraffin-embedded non-diseased NAFLD- or NASH-diagnosed human liver tissue, retrieved from the archives and the biobank of the Department of Pathology and Molecular Pathology, University Hospital Zurich, University Hospital Würzburg and in the setting of the HEP-CAR consortium (Institute for Research in Biomedicine (IRB) Barcelona). Tissues were examined by certified liver pathologists (A.W., J.M.L.). These studies were approved by the local ethics committee (‘Kantonale Ethikkommission Zürich’, application numbers StV26/2005 and KEK-ZH-Nr. 2013-0382) or the Institute for Research in Biomedicine (IRB) Barcelona, Hospital Clinic HCB/2015/0789. In line with the regulation of KEK, individual informed consent from all patients was not required for this kind of retrospective analysis on patients’ material.

The prospective clinical trial has been listed at the German Clinical Trials Register (DRKS), evaluated and accepted by the local ethical authorities (Ethik-Kommission Universitätsklinikum Tübingen) with the ID 587/2016BO2, under the name ‘Platelet inhibition to recues formation of non-alcoholic steatohepatitis in cardiovascular patients’ (Prometheus—prospective, monocenter, observational study).

Prospective trial, ethics, MRI and ultrasound analyses.

The case study of 24 individual observations prospective trial was approved by the institutional ethics committee (587/2016BO2) and complies with the declaration of Helsinki and the good clinical practice guidelines[63–66].

Author Manuscript Author Manuscript Author Manuscript Author Manuscript

For the prospective, ongoing case study, we have included only patients (n = 23) with diabetes mellitus type II and/or body mass index >30, two risk factors, that are highly correlated with development of NAFLD or NASH. All patients underwent cardiac catheretization due to suspected coronary artery disease (CAD). Patients received no antiplatelet treatment if CAD was excluded. Patients received antiplatelet therapy with 100 mg acetylsalicylic acid (ASA) once daily if CAD was present but coronary stent implantation was not indicated. Patients received dual antiplatelet therapy with ASA 100 mg once daily and P2Y12 inhibitor (clopidogrel 75 mg once daily, ticagrelor 90 mg twice daily or prasugrel 10 mg once daily) depending on acuity and severity of CAD (e.g., myocardial infarction versus stable CAD). None of the patients included received long-term treatment with ASA or P2Y12 before study inclusion.

All patients remained on the respective treatment regimens until follow-up. All patients underwent liver MRI and liver ultrasound at baseline (within 4 weeks after hospital discharge) and after 6 months of follow-up. The serum from all patients was analyzed for classic liver damage parameters like AST, ALT, bilirubin, GGT, etc. Additional measurements were performed to exclude reasons other than NAFLD for liver damage, e.g., immune hepatitis, viral hepatitis and AFLD. All patients underwent the Michigan Alcoholism Screening Test to evaluate drinking habits. Patients with left ventricular ejection fraction <45% or severe valve diseases were not included in the study due to the risk of liver congestion.

The hepatic lipid accumulation was quantified by 3T MRI (Skyra, Siemens Healthcare, Erlangen, Germany) at the Department of Diagnostic and Interventional Radiology of the University Hospital of Tübingen, Germany. A commercially available multi-echo Dixon sequence (LiverLab, Siemens Healthcare, Erlangen, Germany) was used, allowing the computation of proton density fat fraction maps and inline segmentation of the liver. Ultrasound examinations in patients were performed twice, at the time of patient recruitment and 6 months after patient recruitment. In order to identify patients presenting with signs of liver steatosis or with signs of liver cirrhosis, bright hepatic echos, increased hepatorenal echogenicity, presence of nodular liver morphology and signs of portal hypertension (e.g., splenomegaly, ascites or intra-abdominal varices) were analyzed using an Aplio 500/T1 (Toshiba)/Ultrasonic transducer 3–5 MHz.

The multivariate analysis (age, gender, anti-aggregation and new statin treatment) to identify statin administration as a possible confounder of the observed effects, patients were differentiated into groups, that received statin treatment prior to hospital admission and those that received new statin treatment at hospital discharge prior to the first MRI examination. We performed a linear regression analysis.

For further details regarding the human samples, please refer to Supplementary Tables 1a,b and 2.

Cholesterol measurements.

Hyperlipidemia is defined as baseline LDL cholesterol ≥160 mg/dl and triglycerides ≥200 mg/dl. Interestingly, only three of the patients of the prospective cohort had triglyceride

Author Manuscript Author Manuscript Author Manuscript Author Manuscript

values ≥200 mg/dl. However, all patients of the prospective cohort showed significantly elevated liver fat accumulation, indicating that patients might not need elevated serum lipid levels to develop fatty liver disease. According to our measurements, only three patients of the prospective trial fulfill the diagnosis hyperlipidemia. However, we decided to include patients with pre-existing conditions, e.g., diagnosis by family doctor, because serum lipid undergoes dynamic regulations. This explains the discrepancy between hyperlipidemia and measured lipid levels in baseline Table 2.

Isolation of liver leukocytes for in-depth myeloid characterization.

Livers were perfused once with PBS, then digested via collagenase at 37 °C for 40 minutes (collagenase type IV, Worthington, UK). Additionally, 0.1 mg/ml DNase I was added after 20 min. Single-cell suspension was obtained by filtering the digested liver through a 70-μm mesh. Hepatocytes were removed by low-speed centrifugation (50 r.c.f., 1 min), and density gradient centrifugation was performed using 18% Nycodenz dissolved in Gey's Balanced Salt Solution (GBSS) as previously described[67].

Cells were then stained for CD206 (C068C2, 141708), CX3CR1 (SA011F11, 149031), CD3 (17A2, 100218), MHCII (M5/114.15.2, 107632) (all BioLegend); CD11b (M1/70, 48-0112-82), F4/80 (BM8, 25-4801-82) (all Invitrogen); CD86 (GL-1, eBioscience, 12-0862-82); CD45 (30-F11, 557659), Ly6G (RB6-8C5, 566218), Ly6C (1A8, 562737) CD11c (HL3, 562949), CD31 (MEC13.3, 565097), NK1.1 (PK136, 557391), TIM-4 (RMT4-54, 564147) (all BD Bioscience), and then multicolor flow cytometry was run using an LSR Fortessa (BD Biosciences). Analysis was done using FlowLogic (v7.2, Inivai, Australia) and FlowJo (v10.4, BD Biosciences). Additionally, liver MoMF and Kupffer cells were sorted for NanoString gene expression analysis using an Aria-II (BD Biosciences).

For details regarding the definitions of violin plot elements of Supplementary Fig. 3i, refer to Supplementary Table 3.

t-distributed stochastic neighbor embedding (t-SNE).

Liver leukocytes were pregated for living (7-AAD-), $CD45^+$, $Ly6G^-$, $CD31^-$, $F4/80^+$ cells by using FlowJo (v10.4, BD Biosciences), then t-SNE-based clustering was done as described previously[68], using the Rtsne package for R. Clusters were identified by hierarchical clustering and projected onto the two-dimensional t-SNE plot, while relative protein expression was displayed for each cluster by violin plots using R (v3.5.1).

nCounter gene expression analysis.

Gene expression analysis of 561 selected gene targets of liver MoMF and Kupffer cells was performed using NanoString assays (nCounter Mouse Immunology Kit, NanoString Technologies). Analysis was done using the nSolver Software (v2.0, NanoString Technologies). PCA was done using the prcomp package for R (v3.5.1).

Measurement of serum parameters.

Serum was isolated from mice and liver enzymes AST and ALT were quantified using the Roche Modular System (Roche Diagnostics) with a commercially available automated

Author Manuscript Author Manuscript Author Manuscript Author Manuscript

colorimetric system at the Institute of Clinical Chemistry at the University Hospital Zurich using a Hitachi P-Modul (Roche). Total cholesterol was measured in a 96-well format using CHOL or TG GPO-PAP substrates (Roche Diagnostics).

Measurement of liver triglycerides.

Liver-specific triglyceride levels were analyzed from snap frozen liver tissue samples. Liver tissue samples were homogenized in sodium chloride (0.9 % NaCl), and liver-resident lipids were precipitated using ethanolic potassium hydroxide (0.5 M KOH) and solubilized in magnesium sulphate (0.15 M $MgSO_4$). The concentration of hepatic triglycerides was then measured using triglycerides GPO-PAP from Roche Diagnostics on a spectrophotometer at 505 nm.

Intraperitoneal glucose tolerance test.

Intraperitoneal glucose tolerance tests were carried out on mice fasted overnight for 16 h. Basal blood glucose concentrations were determined for each mouse prior to glucose (2 mg/g body weight) administration using a hand-held glucose analyzer (FreeStyle Freedom Lite; Abbott). Each mouse then received glucose via intraperitoneal injection, and blood glucose concentrations were subsequently remeasured 15, 30, 60 and 120 min post glucose administration.

Intraperitoneal insulin tolerance test and fasting insulin determination.

Intraperitoneal insulin tolerance tests were carried out on mice mild fasted for 6 h. Basal blood glucose concentrations were determined for each mouse prior to insulin (1U/g lean mass determined by EchoMRI analysis) administration using a hand-held glucose analyzer (FreeStyle Freedom Lite; Abbott). Each mouse then received Insulin via intraperitoneal injection and blood glucose concentrations were subsequently re-measured 15, 30, 60 and 120 min post glucose administration. Fasted insulin levels were measured in mildly fasted (8 h) mice using the ALPCO mouse insulin ELISA kit.

Immunoblot analysis.

Liver homogenates were prepared in a pH 7.4 lysis buffer containing 1% NP-40 (Sigma-Aldrich, Gillingham, UK), 50 mmol/L Tris, 10% glycerol, 0.02% NaN3, 150 mmol/L NaCl, and a cocktail of phosphatase and protease inhibitors (Sigma-Aldrich), and protein concentration was determined using the Pierce BCA Protein Assay Kit (Thermo Scientific) according to the manufacturer's manual. Liver homogenates were prepared using a homogenizer. Tissue preparation was performed with gentleMACS Octo Dissociator (Miltenyi Biotec). 20–80 μg of proteins were separated under reducing conditions (2.5% β-mercaptoethanol) by gel electrophoresis (Mini Protean Gels, Bio Rad) and blotted by semi-dry blotting (Trans-Blot Turbo Transfer, Bio Rad) onto nitrocellulose membranes (Bio Rad). Membranes were blocked in 5% milk/PBS-T for at least 1 h at RT. Primary antibodies against P-p38MAPK ((Thr180/Tyr182) D3F9, 4511), p38 MAPK (D13E1, 8690), P-p65 (Ser536, 3033), p65 (D14E12, 8242), COX2 (D5H5, 12282), GAPDH (14C10, 2118) (all Cell Signaling) were incubated at 4 °C overnight under shaking conditions. Incubation with the secondary antibody (HRP-anti-rabbit IgG, 1:5000; Promega, W4011) was performed

Author Manuscript Author Manuscript Author Manuscript Author Manuscript

under shaking conditions for 1 h. Detection was achieved using Clarity Western ECL Substrate (Bio Rad) with the Stella 3200 imaging system (Raytech).

Flow cytometry.

For flow cytometry analysis, antibodies against CD8-α (53-6.7, 100734), CD3-ε (500A2, 152314), CD19 (6D5, 115530), NK1.1 (PK136, 108710), were purchased from BioLegend. Antibodies against CD4 (RM4-5, 11-0042-82) and Foxp3 (FJK-16s, 17-5773-82) were purchased from eBioscience. Viability was assessed by LIVE/DEAD Fixable Aqua or ZombieDyeNIR (Life Technologies). TA99 was labeled with an Alexa Fluor 647 NHS Ester (Life Technologies, MA1-25303) to generate TA99-647. Further antibodies that were used include CD44 (clone IM7, BioLegend, diluted 1:200, 103012), CD69 (clone H1.2F3, BioLegend, diluted 1:200, 104508), CD62L(clone MEL-14, BioLegend, diluted 1:200, 104448). Intracellular cytokine staining (ICS) was performed as described previously[11]. Peptides used for restimulation were 10 μg/ml of the relevant antigen: Trp2180-188 (SVYDFFVWL), Her2/Neu66-74 (TYVPANASL), Tyrp-1455-463native (TAPDNLGYA), or gp10025-33native (EGSRNQDWL). Cells were analyzed using BD FACS LSR II, BD FACS LSR Fortessa, BD FACSCanto, and Sony spectral analyzer SP6800 flow cytometers, and data were analyzed using FlowJo.

Histology, immunohistochemistry, scanning and automated analysis.

Liver samples were fixed in 4% paraformaldehyde and paraffin-embedded at the University Hospital Zürich, Department of Pathology and Molecular Pathology Core, at the Technical University of Munich (TUM), or at the DKFZ, Department of Chronic Inflammation and Cancer (Heidelberg) as described[11]. Briefly, 2 μm sections from FFPE and cryo-preserved tissues were prepared and stained with Hematoxylin/Eosin or IHC antibodies. Incubation in Ventana buffer and staining was performed on a NEXES immunohistochemistry robot (Ventana Instruments) using an IVIEW DAB Detection Kit (Ventana) or on a Bond MAX (Leica). For Sudan Red staining, cryo sections (5 μm) were cut and stained with Sudan Red (0.25% Sudan IV in ethanolic solution). Slides were scanned with a Nano Zoomer (Hamamatsu, Japan).

Antibodies that were used included anti-MHCII, rat, 1:500 (clone M5/114.15.2, NBP1-43312); anti-CD3, rabbit, 1:250 (clone SP7, Abcam, ab16669); and anti-F4/80, rat, 1:50 (BioLegend, BM8, cat. no. 123105). Further antibodies used included collagen IV, rabbit 1:50 (Cedarlane, clone CL50451AP-1, 007CL50451AP); Ki67, rabbit 1:200 (Thermo Scientific, clone RM-9106-S1, RM-9106-S1); B220, rat 1:3000 (BD, clone RA3-6B2, 553084); Ly6G rat 1:600 (BD, clone 1A8, 551459), PERK1/2, rabbit, 1:400 (Cell Signaling, clone D13.14.4E, 4370); glutamine synthethase (GS) rabbit 1:500 (Abcam, ab16802); PSTAT3, rabbit, 1:100 (Cell Signaling clone D3A7, 9145); and CD42b, rabbit, 1:200 (Abcam, clone SP219, ab183345).

For quantification of stains, slides were scanned using a SCN400 slide scanner (Leica) and analyzed using Tissue IA image analysis software (4.0.6 Slidepath, Leica). For quantification of platelet staining on human (CD61) and mouse (CD42b) tissue, software-

Author Manuscript Author Manuscript Author Manuscript Author Manuscript

based analysis and counting at the screen (CD42b; 100 high-power fields; 40×) were performed.

For Sudan red^{+} liver area, data are presented as Sudan red–positive area in percent of total tissue area. Three random liver tissue areas of approximately 6–8 mm^2 (87,000 μm^2) were selected in DIH (digital image hub, Leica), submitted to analysis and merged.

NAFLD activity score (NAS) was applied to murine livers.

Electron microcopy.

For electron microscopy, sections from epon-embedded, glutaraldehyde-fixed liver samples were cut and stained with toluidine blue. The tissue was trimmed, and ultrathin cross sections of the liver were cut and treated with uranyl acetate and lead citrate as described previously[69]. Electron micrographs were analyzed for cell composition and localization using the analySIS Docu System (Soft Imaging System).

Preparation of mouse platelets.

Blood was obtained from the tail of each mouse and drawn into citrate tubes at a 1:10 ratio. Platelet-rich plasma (PRP) was obtained by centrifugation at 260*g* for 5 min. Afterward, platelet-rich plasma was centrifuged at 640*g* for 5 min to pellet the platelets. After two washing steps, the pellet of washed platelets was resuspended in modified Tyrode-HEPES buffer (pH 7.4, supplemented with 1 mM $CaCl_2$).

Platelet aggregometry.

Washed platelets were adjusted to a concentration of 150 × 10^3 platelets/μl in Tyrode-HEPES buffer (pH 7.4 supplemented with 1 mM CaCl2). Aggregation was estimated from light transmission determined with a luminoaggregometer model 700 (ChronoLog, Havertown, PA, USA). Following calibration, agonists including adenosine 5′-diphosphate (ADP), U46619 (U46), thrombin (Thr), collagen-related peptide (CRP), rhododcytin (RC) were added at the indicated concentrations, and aggregation was measured for 10 min with a stir speed of 1,000 r.p.m. at 37 °C. Afterward, analysis was performed using the aggrolink8 software (ChronoLog).

Analysis of platelets and flow cytometry of platelets.

Mice were bled under isoflurane anesthesia. Blood was collected in a tube containing 20 U/ml heparin, and PRP was obtained by two cycles of centrifugation at 300*g* for 6 min at room temperature. For preparation of washed platelets, PRP was washed twice at 800*g* for 5 min at RT, and the pellet was resuspended in modified Tyrodes-HEPES (N-2-hydroxyethyl-piperazone-N′2-ethanesulfonic acid) buffer (134 mM NaCl, 0.34 mM Na_2HPO_4, 2.9 mM KCl, 12 mM $NaHCO_3$, 5 mM HEPES, 1 mM $MgCl_2$, 5 mM glucose, 0.35% BSA, pH 7.4) in the presence of prostacyclin (0.1 μg/ml) and apyrase (0.02 U/ml).

Apyrase grade III (Sigma-Aldrich), prostacyclin (PGI2), ADP (Sigma-Aldrich), U-46619 (Enzo Life Sciences), thrombin (Roche), rabbit anti-human VWF (DAKO), rabbit anti-human fibrinogen (DAKO) were purchased as indicated. CRP and rhodocytin were

Author Manuscript Author Manuscript Author Manuscript Author Manuscript

generated and isolated as previously described[36]. The antibody against the activated form of integrin αIIbβ3 (JON/A-PE) was from Emfret Analytics. Other antibodies we received, listed below, were generated in the laboratory of B.N.

Antibody	Clone	Isotype	Antigen	Reference
JON/A	4H5	IgG2b	αgG2be	70
WUG 1.9	5C8	IgG1	P-selectin	71
JAQ1	98A3	IgG2a	GPVI	72
LEN1	12C6	IgG2b	α2	73
ULF1	96H10	IgG2a	CD9	74
p0p4	15E2	IgG2b	GPIb	74
p0p6	56F8	IgG2b	GPIX	74
JON2	14A3	IgG2b	αIIbβ3	74
DOM2	89H11	IgG2a	GPV	74
INU1	11E9	IgG1	CLEC-2	75

RNA isolation and quantitative real-time PCR.

Total RNA was isolated from snap frozen liver tissues according to the manufacturer's protocol using RNeasy Mini Kit (Qiagen). The quantity and quality of the RNA were determined spectroscopically using a Nanodrop analyzer (Thermo Scientific). 1 μg of purified RNA was subsequently transcribed into cDNA using Quantitect Reverse Transcription Kit (Qiagen) according to the manufacturer's protocol. Quantitative RT-PCR was performed using Fast Start SYBR Green Master Rox (Roche). Primers were custom made by Microsynth as previously described[11]. For mRNA expression analysis, quantitative real-time PCR was performed in duplicates in 384-well plates using Fast Start SYBR Green Master Rox (Roche) on a 7900 HT qRT-PCR system (Applied Biosystems, Life Technologies Darmstadt, Germany). Relative mRNA levels were calculated according to the $\Delta\Delta C_t$ relative quantification method and were normalized to levels of a housekeeping gene (GAPDH or ROTH2). The data were normalized to the expression of the housekeeping gene and analyzed using GraphPad Prism software version 7.03 (GraphPad Software). For the analysis of whole liver homogenates by microarray (Agilent), the following genes were selected, analyzed and shown. For a list of all used primers for RT-qPCRs, refer to Supplementary Table 4.

Gene expression profiling.

Transcriptional profiling was performed using SurePrint G3 Mouse Gene Expression 8 × 60 k microarrays (Agilent Technologies, AMADID 28005) according to the manufacturer's protocol. 75 ng of total RNA was used in labeling using the Low Input Quick Amp Labeling Kit (one-color, Agilent Technologies). Raw gene expression data were extracted as text files with the Feature Extraction software 11.0.1.1 (Agilent Technologies). The expression microarray data were uploaded to ArrayExpress (www.ebi.ac.uk/arrayexpress/), and the data set is available under the accession number E-MTAB-6073, entitled 'Transcriptomic differences in livers of mice fed with normal diet and choline-deficient high-fat diet'.

Author Manuscript Author Manuscript Author Manuscript Author Manuscript

All data analysis was conducted using the R statistical platform (version 3.2.2, www.r-project.org). Data quality assessment, filtering, preprocessing, normalization, batch correction based on nucleic acid labeling batches and data analyses were carried out with the Bioconductor R-packages limma, Agi4×44PreProcess and the ComBat function of the sva R-package. All quality control, filtering, preprocessing and normalization thresholds were set to the same values as suggested in Agi4×44PreProcess R-package user guide. Only HGNC annotated genes were used in the analysis. GSEA was conducted on calculated $\log_2$-expression values of all array probes using the 'GSEA Pre-ranked' function with default settings[76].

RNA sequencing.

Library preparation for bulk 3′-sequencing of poly(A)-RNA was done as described previously[77]. Briefly, barcoded cDNA of each sample was generated with a Maxima RT polymerase (ThermoFisher) using oligo-dT primer containing barcodes, unique molecular identifiers (UMIs) and an adapter. 5′ ends of the cDNAs were extended by a template switch oligo (TSO); after pooling of all samples, full-length cDNA was amplified with primers binding to the TSO-site and the adapter. cDNA was tagmented with the Nextera XT kit (Illumina) and 3′-end-fragments finally amplified using primers with Illumina P5 and P7 overhangs. In comparison to Parekh et al.[77], the P5 and P7 sites were exchanged to allow sequencing of the cDNA in read1 and barcodes and UMIs in read2 to achieve a better cluster recognition. The library was sequenced on a NextSeq 500 (Illumina) with 75 cycles for the cDNA in read1 and 16 cycles for the barcodes and UMIs in read2.

RNA sequencing analysis.

Gencode gene annotations version M18 and the mouse reference genome GRCm38.p6 were derived from the Gencode homepage (https://www.gencodegenes.org/). Dropseq tools v1.12 (ref. [78]) was used for mapping the raw sequencing data to the reference genome. The resulting UMI filtered countmatrix was imported into R v3.4.4. Prior differential expression analysis with DESeq2 1.18.1 (ref. [79]), dispersion of the data was estimated with a parametric fit including the dietary status of the mice as explanatory variable in the model. The Wald test was used for determining differentially regulated genes between the high-fat and normal diet group and shrunken $\log_2$ fold changes were calculated afterward, with setting the type argument of the lfcShrink function to 'normal'. A gene was determined to be differentially regulated if the absolute $\log_2$ fold change was greater than 1 and the adjusted *P* value was below 0.05. Gene set enrichment analysis was conducted with EnrichR[80] within the Reactome database. Raw sequencing data are available under the accession number MTAB-7625.

MRI analysis for mice.

Steatosis was analyzed in 6-month-old B6 mice fed with ND, CD-HFD or CD-HFD/Asp-Clop treated groups. A Pharmascan 7 T MRI (Bruker) with Paravision 5.1 software was used in FLASH scan mode without fat suppression using an echo-time of 2.2 ms for out-phase and 2.9 ms for in-phase based on previous reports[81,82].

Author Manuscript Author Manuscript Author Manuscript Author Manuscript

Calorimetric TSE analysis.

Mice were individually housed for indirect calorimetry in PhenoMaster (TSE systems). Mice were allowed to acclimate to the new environment for at least 2–3 d, then metabolic parameters were measured, such as food and water intake, O_2 consumption, CO_2 production, respiratory exchange ratio and total activity. All parameters were measured for at least 4 consecutive d with five measurement values every hour. Analysis of covariance (ANCOVA) was first conducted to ensure that body weight does not play a significant effect on the measured parameters.

Immunofluorescence microscopy of liver sections.

To achieve rapid fixation after euthanasia, livers were fixed with paraformaldehyde–lysine–periodate (PLP) for 4–8 h, rehydrated in 30% sucrose solution for 48 h and snap frozen in OCT (Cell Path). Thick (5 μm) cryosections were obtained using a Leica Cryostat and the Cryojane tape transfer system (Leica Microsystems).

Generation of liver slices for confocal microscopy.

The generation of the liver slices for microscopy was performed and adapted from a previously described protocol[83]. Briefly, livers were collected and processed as described above. OCT-embedded frozen livers were iteratively sectioned using a cryostat. Samples were then reversed and the procedure was repeated on the opposite face of the liver until a 30-μm-thick slice of liver was obtained. OCT freezing medium covering the sample was removed, and slices were washed with PBS and blocked overnight at 4 °C in blocking solution (0.2% Triton/1%BSA/10% donkey serum/PBS). Liver slices were stained with rat anti-CD41, goat anti-CD105, rabbit anti-Col IV and rabbit anti-CD8 for 3 d in blocking solution, washed overnight in PBS and stained with DyLight488 donkey anti-rabbit IgG and DyLight549 or DyLight649 donkey anti-rat IgG. Stained slices were then washed in PBS and incubated overnight in FocusClear (CelExplorer Lab). For observation under the confocal microscope, liver slices were embedded in FocusClear and mounted on glass slides.

Immunofluorescence staining.

Livers were perfused with PBS through inferior vena cava, harvested and fixed in 4% paraformaldehyde for 16 h, then dehydrated in 30% sucrose prior to embedding in OCT freezing media (Sakura). 25-μm sections were cut on a HM550 cryostat (ThermoFisher) and adhered to Superfrost Plus slides (Thermo Scientific). Sections were then permeabilized and blocked in PBS containing 0.3% Triton X-100 (Sigma-Aldrich) and 10% FBS, then stained in the same blocking buffer. The following primary antibodies were used for staining: rabbit anti-collagen IV (1:200 Abcam, 10808); CD41 PE (1:100 MWReg-30 BioLegend, 133906), rat anti-F4/80 APC (1:100 BM8 ThermoFisher, 17-4801-82), rabbit anti-CD3 (1:100 DAKO A0445229-2), B220 AF 647 (1:100 RA3-6B2 BioLegend, 103226), CD11b APC (1:100 M1/70 BioLegend, 101212). Stained slides were mounted with fluorescence mounting medium (DAKO), and images were acquired on an inverted Leica microscope (TCS STED CW SP5, Leica Microsystems) with a motorized stage for tiled imaging.

To minimize fluorophore spectral spillover, we used the Leica sequential laser excitation and detection modality. The bleed-through among sequential fluorophore emission was

Author Manuscript Author Manuscript Author Manuscript Author Manuscript

removed by applying simple compensation correction algorithms to the acquired images. The semiautomatic surface-rendering module in Imaris (Bitplane) was used to create 3D volumetric surface objects corresponding either to individual cells or to the liver sinusoids. Signal thresholds were determined using the Imaris Surface Creation module, which provides automatic threshold identification and value-based visual surface thresholding around the positively stained objects.

For the semi-quantitative analysis of platelet adhesion to liver sinusoids, high-resolution confocal *x*–*y*–*z* stacks of 30 *x*–*y* sections (1,024 × 1,024 pixels) sampled with 0.5 μm *z* spacing were acquired to provide image volumes of 388 × 388 × 30 μm^3. The confocal *z* stacks were imported into Imaris software (Bitplane), and platelets were reconstructed as 3D volumes by means of the semiautomatic surface-rendering module with a seed point diameter of 2.08 μm (the mean platelet diameter[84,85]). The split touching objects option of the module supports the separation of two or more objects that are identified as one, enabling the splitting of aggregates into single components. All analysis was performed at least on 12 random fields of view (FOV).

Confocal imaging analysis.

For platelet aggregate size analysis, the surface and volume of each single platelet aggregate (containing more than two single platelets) from at least 12 different FOV was automatically obtained from the surface-rendering module (imaris, Bitplane); The PLT/endothelium coverage was derived from the same FOV as percentage of the total sinusoidal surface (calculated in each FOV) covered by PLT.

For quantification of the immune cell–PLT interaction, the immune cells ($CD3^+$, $CD11b^+$ and $B220^+$) adjacent and non-adjacent to PLT were manually counted in 12 FOV. The interaction was expressed as total number of adjacent cells as well as percentage of cells adjacent to PLT over the total number of cells.

The $CD3^+$ cells/PLT interaction was further analyzed by calculating, for each cell, the contact surface area between them.

Multiplex ELISA.

Cytokines and chemokines in whole liver of ND, CD-HFD and Asp-Clo-treated CD-HFD mice (12 months old) were evaluated using a laser bead technology–based Mouse Cytokine Array Chemokine Array 31-Plex (MD31) by Eve Tech (Eve Technologies, Calgary, AB, Canada).

Cytokine profiler.

Cytokines and chemokines in whole liver of ND, CD-HFD/ctrl ab and CD-HFD/anti-GPIbα antibody mice (6 months old) or in CD-HFD and CD-HFD/*hIL4Rα/GPIbα*-Tg mice (12 months old) were assessed using the Mouse XL Cytokine Array Kit by R&D Systems.

Author Manuscript Author Manuscript Author Manuscript Author Manuscript

Spinning-disc microscopy.

All imaging experiments were performed using 7- to 12-week-old male mice. All mice were co-housed and bred in a specific-pathogen-free facility at the University of Calgary with a 12 h light/dark cycle and access to food and water ad libitum.

Preparation for intravital Microscopy.

Multichannel spinning-disk confocal microscopy was used to image the liver as previously described (Surewaard and Kubes 2017). Briefly, mice were anesthetized by intraperitoneal injection of ketamine (200 mg/kg body weight; Bayer Animal Health) and xylazine (10 mg/kg body weight; Bimeda-MTC). A catheter was inserted into the tail vein to allow administration of fluorescently conjugated antibodies, proteins and additional anesthetics. A midline and lateral abdominal incision were made, and the abdominal wall was partly removed to access the liver. The mouse was placed in a right lateral position on a heating plate to maintain body temperature at 37 °C. The liver was exteriorized onto a glass coverslip and covered with moisturized laboratory tissues to restrict movement and breathing artefacts. Abdominal organs were covered with saline-soaked gauze to prevent dehydration.

Intravital microscopy.

Image acquisition of the liver was performed using an inverted spinning-disk confocal microscope (IX81; Olympus), equipped with a focus drive (Olympus) and a motorized stage (Applied Scientific Instrumentation). The microscope was fitted with a motorized objective turret equipped with 43/0.16 UPLANSAPO, 103/0.40 UPLANSAPO, and 203/0.70 UPLANSAPO objective lenses. The microscope was linked with a confocal light path (WaveFx; Quorum Technologies) based on a modified CSU-10 head (Yokogawa Electric Corporation). Cells of interest were visualized using fluorescently conjugated antibodies. Volocity software (Perkin Elmer) was used to drive the confocal microscope and for acquisition and analysis of images.

Antibodies for intravital imaging.

Antibodies for intravital imaging were as follows: Alexa Fluor (AF) 750–conjugated anti-mouse F4/80 (2 μg/mouse; clone BM8; AbLab, custom made), Alexa Fluor (AF) 647–conjugated anti-mouse CD49b (3 μg/mouse; clone HMa2; BioLegend, 103511), PE-conjugated anti-mouse Ly6G (3 μg/mouse; clone 1A8; BioLegend, 127607) and FITC-conjugated anti-mouse CD3e (2 μg(mouse; clone 145-2c11; eBioscience, 11-0031-82). HAPB (Sigma-Aldrich) was fluorescently (Alexa Fluor 555; Invitrogen) conjugated and injected intravenously to detect intrahepatic HA.

In vivo treatments.

Kupffer cell depletion was performed by intravenous injection of 100 μl Clodronate (17 mM) twice a week for 2 weeks. Hyaluronidase (Sigma-Aldrich) was given by intraperitoneal injection twice a week at a dose of 20U/g per mouse for 2 weeks. The last dose was given 3 h before intravital imaging.

Author Manuscript Author Manuscript Author Manuscript Author Manuscript

In vivo image analysis.

All videos and images were acquired and processed using Volocity software (PerkinElmer). Quantification of platelet aggregation, Kupffer cell and neutrophil numbers and sinusoid diameters were also performed using Volocity software. For each mouse, ten FOV were randomly selected and assessed. Platelet aggregation was measured using the 'find objects' function in Volocity software and the highest background was subtracted as described (Surewaard et al 2018). Kupffer cell and neutrophil numbers were manually counted in ten randomly selected FOV. For measurement of sinusoidal diameter, images were exported from Volocity software as.jpg files. ImageJ software (NIH) was used to measure sinusoid diameters. For each mouse, we measured ten randomly selected sinusoids in five FOV.

Statistical analyses.

Mouse data are presented as the mean ± s.e.m. Pilot experiments and previously published results were used to estimate the sample size such that appropriate statistical tests could yield significant results. Statistical analysis was performed using GraphPad Prism software version 7.03 (GraphPad Software). Data of three or more groups were analyzed by analysis of variance with the post hoc Tukey's or Bonferroni multiple comparison test. Data for the three groups over time were analyzed by two-way analysis of variance with the post hoc Tukey's multiple comparison test. Analysis of two samples was performed with two-tailed Student's *t* test and the Mann–Whitney *t* test, and statistics for HCC incidence were calculated using two-tailed Fisher's exact test. Statistical significance is indicated either as exact *P* value or as follows:* $P < 0.05$, ** $P < 0.01$, *** $P < 0.001$, and **** $P < 0.0001$; 'n.s.' indicates not significant.

Moreover, the data that support the findings of this study are available from the corresponding authors upon reasonable request. If not stated otherwise, the authors declare that all other data supporting the findings of this study are available within the paper and its supplementary information files.

Fig. 6a and Supplementary Fig. 12 have associated source data that are uploaded to ArrayExpress (www.ebi.ac.uk/arrayexpress/) and the data set is available under the accession number E-MTAB-6073, entitled 'Transcriptomic differences in livers of mice fed with normal diet and choline-deficient high-fat diet'.

Reporting Summary.

Further information on research design is available in the Nature Research Reporting Summary linked to this article.

Author Manuscript Author Manuscript Author Manuscript Author Manuscript

Extended Data

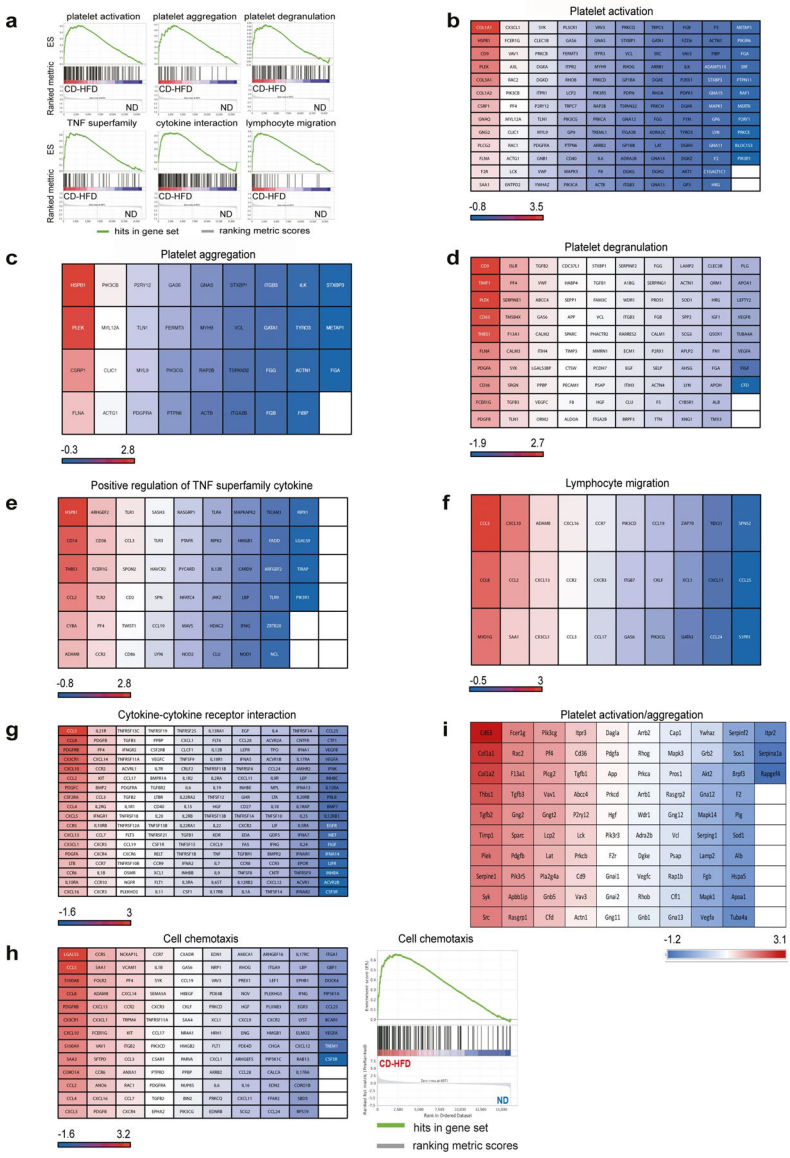

Extended Data Fig. 1 |. Transcriptional alterations in the course of NASH and physical interaction of immune cells, liver endothelium and platelets.

a. GSEA and expression analysis of genes related clusters of platelet activation, aggregation, degranulation and genes associated to TNFα family regulation, cytokine interaction and lymphocyte migration from 6 months ND-fed versus CD-HFD-fed mice. **b**–**g**, Gene expression alterations found in annotated genes of indicated clusters and mice shown in **a**. **h**, Gene expression alterations found in annotated genes of indicated cluster of cell chemotaxis (left) and GSEA and expression analysis of genes associated to the cell chemotaxis cluster from mice shown in **a** (right). **i**, Transcriptional alterations for genes associated with platelet activation/aggregation of the 7.5 month ND versus WD-HTF fed mice.

Author Manuscript Author Manuscript Author Manuscript Author Manuscript

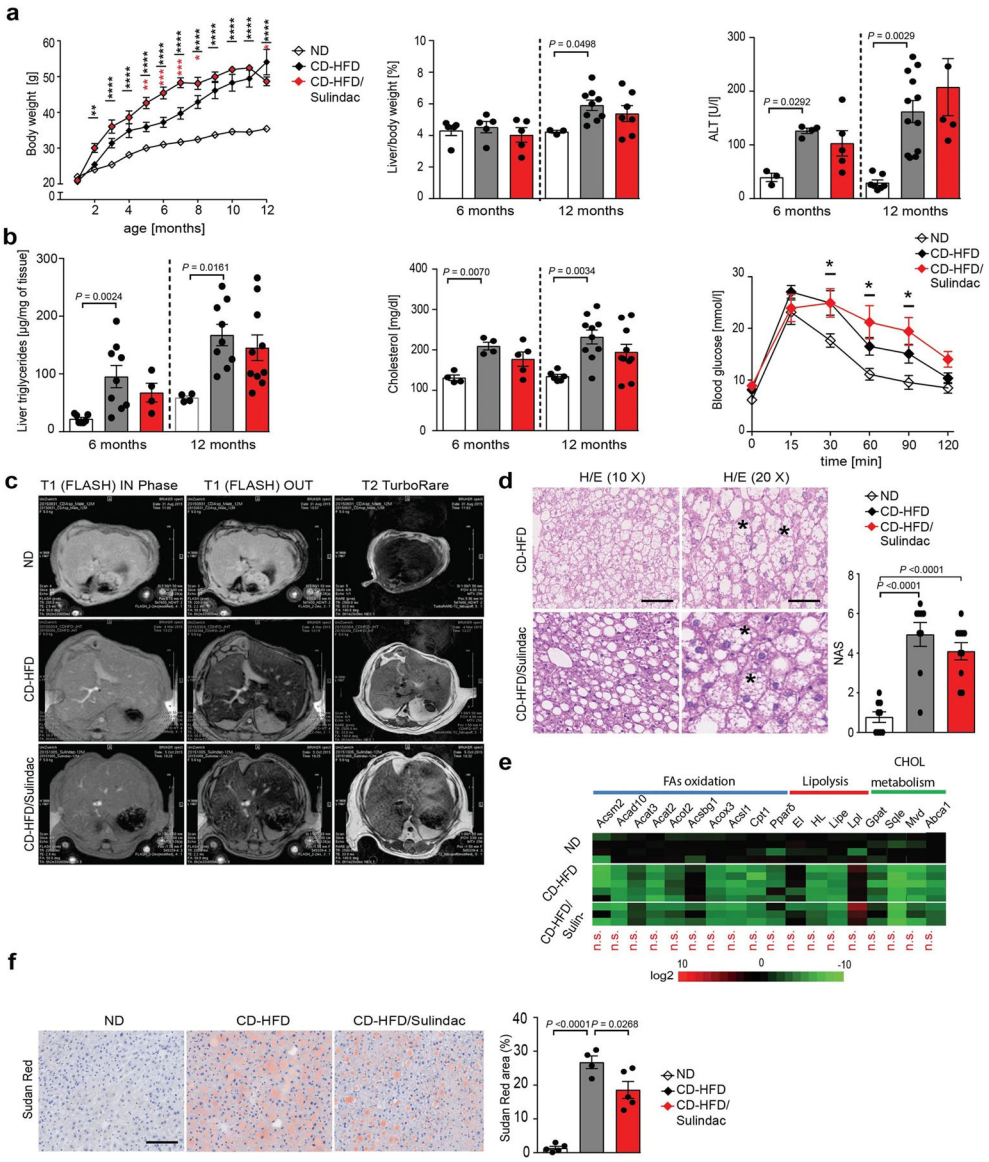

Extended Data Fig. 2 |. Sulindac treatment does not prevent NASH pathology.

a, Left, mouse weight development in 12 months ND-, CD-HFD- or CD-HFD/sulindac-fed mice (n = 5 mice/group). Statistics: ND vs CD-HFD (black asterisks), ND vs CD-HFD/ sulindac (red asterisks). Middle, liver/body weight (6 months: n = 5 mice/group; 12 months: ND n = 3 mice; CD-HFD n = 8 mice; CD-HFD/sulindac n = 7 mice) and (right) ALT levels of 6 and 12 months ND-, CD-HFD- or CD-HFD/sulindac-fed mice (6 months: ND n = 3 mice; CD-HFD n = 4 mice; CD-HFD/sulindac n = 5 mice; 12 months: ND n = 7 mice; CD-HFD n = 12 mice; CD-HFD/sulindac = 5 mice). **b**, (left) Liver triglycerides and (middle) serum cholesterol levels in 6 and 12 months ND-, CD-HFD- or CD-HFD/sulindac-fed mice (liver TGs 6 months: ND = 7 mice; CD-HFD n = 11 mice; CD-HFD/sulindac n = 4 mice; Liver TGs 12 months: ND n= 4 mice; CD-HFD n = 9 mice; CD-HFD/sulindac n = 10 mice; cholesterol 6 months: ND n = 4 mice; CD-HFD n = 4 mice; CD-HFD/sulindac n = 5 mice; cholesterol 12 months: ND n = 6 mice; CD-HFD n = 10 mice; CD-HFD/sulindac n = 10

Author Manuscript Author Manuscript Author Manuscript Author Manuscript

mice). (right) IPGTT performed with 6 months ND-, CD-HFD- or CD-HFD/sulindac-fed mice (n = 5 mice/group). Statistics: ND vs CD-HFD (black asterisks). (c) MRI analyses of livers of 6 months ND-, CD-HFD- or CD-HFD/sulindac-fed mice (n = 3 mice/group). **d**, (left) Analysis by H&E indicate damaged hepatocytes (asterisk) and (right) evaluation by NAS in livers of 6 months CD-HFD- or CD-HFD/sulindac-fed mice (ND n = 9 mice; CD-HFD n = 9 mice; CD-HFD/sulindac n = 10 mice), scale bars: 100 μm in 10×, 50 μm in 20×. **e**, Real-time qPCR analysis for mRNA of genes involved in lipid metabolism in liver of 6 months ND-, CD-HFD- or CD-HFD/sulindac-fed mice (ND n = 4 mice; CD-HFD n = 5 mice; CD-HFD/sulindac n = 3 mice). Comparison between CD-HFD vs CD-HFD/sulindac. **f**, Sudan red staining and quantification for fat accumulation of 6 months ND-, CD-HFD- or CD-HFD/sulindac-fed mice (ND n = 5; CD-HFD n = 4; CD-HFD/sulindac n = 5). Scale bar: 100 μm. All data are shown as mean ± s.e.m. Data in **a** (left) and **b** (right) were analyzed by two-way analysis of variance with post hoc Tukey's multiple comparison test. Data in **a** (middle and right), **b** (left and middle), **d** and **f** were analyzed by one-way analysis of variance with post hoc Tukey's multiple comparison test. Data in **e** were analyzed by two-tailed Mann-Whitney t test. *P < 0.05, **P < 0.01, ***P < 0.001, ****P < 0.0001.

Author Manuscript Author Manuscript Author Manuscript Author Manuscript

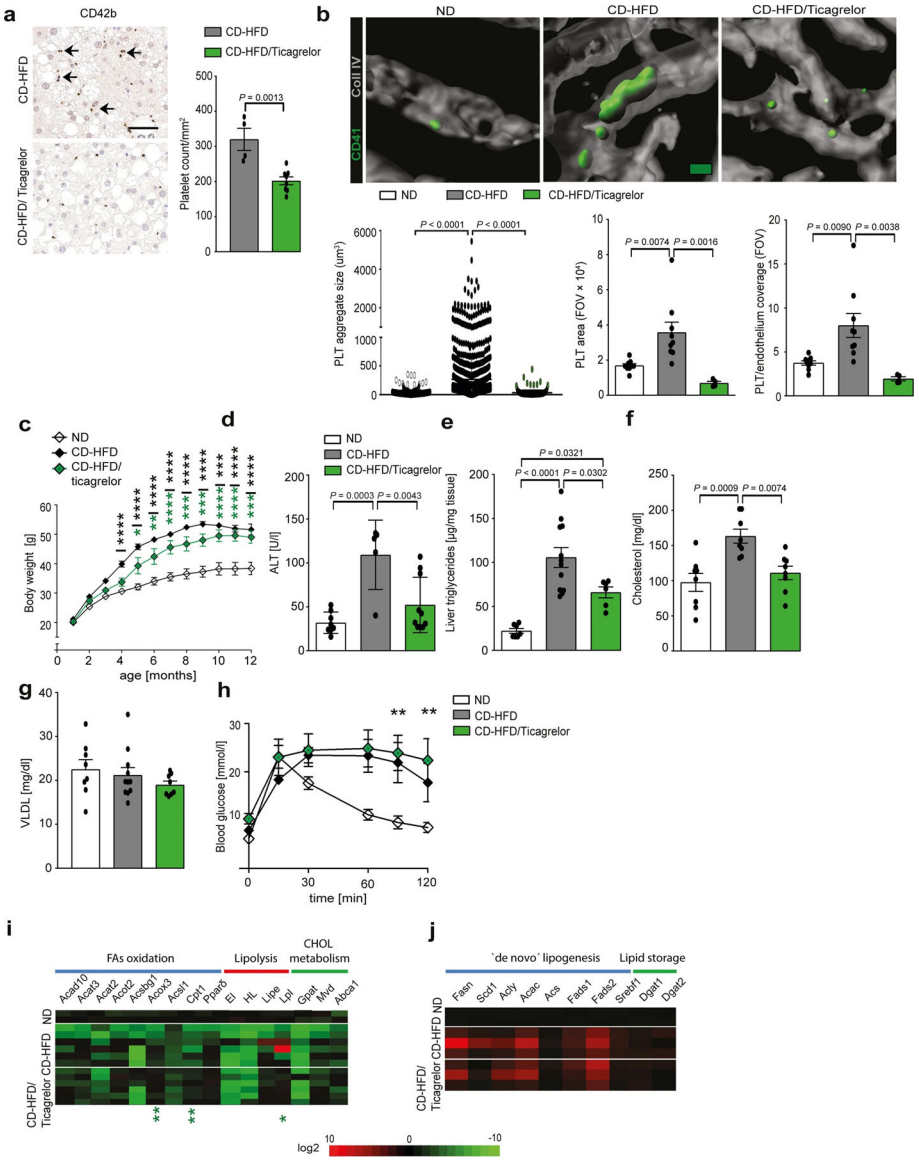

Extended Data Fig. 3 |. Ticagrelor treatment attenuates CD-HFD-induced NASH and NASH-associated conditions, and prevents HCC.

a, CD42b staining and quantification in 6 months CD-HFD or CD-HFD/Ticagrelor fed mice (CD-HFD $n = 4$ mice; CD-HFD/Ticagrelor $n = 8$ mice), scale bar: 50 µm. **b**, 3D confocal images of platelet (green)/liver endothelium (grey) interaction in livers of 6 months ND, CD-HFD and CD-HFD/Ticagrelor fed mice ($n = 4$ mice/group), scale bar: 20 µm. Quantification of platelet (PLT) aggregate size, overall PLT surface and quantification of platelet/liver endothelium coverage in focus of view ($n = 4$ mice/group). For visualization of intravascular events, the transparency of the sinusoidal rendering was set to 50%. **c**, Body weight development in 12 months ND, CD-HFD or CD-HFD/Ticagrelor fed mice (ND $n = 4$ mice; CD-HFD $n = 6$ mice; CD-HFD/Ticagrelor $n = 4$ mice). Statistics: ND vs CD-HFD (black asterisks), ND vs CD-HFD/Ticagrelor (green asterisks). **d**–**h** ALT (**d**), Liver triglyceride (**e**), serum cholesterol levels (**f**), VLDL secretion in serum (**g**) and IPGTT (**h**) of 6 months ND, CD-HFD or CD-HFD/Ticagrelor fed mice (ALT: ND $n = 8$ mice;

Author Manuscript Author Manuscript Author Manuscript Author Manuscript

CD-HFD $n = 5$ mice; CD-HFD/Ticagrelor $n = 10$ mice; liver triglycerides: ND $n = 7$ mice; CD-HFD $n = 11$ mice; CD-HFD/Ticagrelor $n = 6$ mice; serum cholesterol: $n = 8$ mice/group; liver triglycerides: ND $n = 8$ mice; CD-HFD $n = 11$ mice; CD-HFD/Ticagrelor $n = 8$ mice; IPGTT: ND $n = 5$ mice; CD-HFD $n = 3$ mice; CD-HFD/Ticagrelor $n = 3$ mice). **i**,**j**, Real-time qPCR analysis of hepatic genes associated to catabolic (**i**) and anabolic processes (**j**) of lipid metabolism of 6 months ND, CD-HFD or CD-HFD/Ticagrelor fed mice (RT-qPCR for catabolic genes: ND $n = 2$ mice; CD-HFD $n = 6$ mice; CD-HFD/Ticagrelor $n = 6$ mice; RT-qPCR for anabolic genes: ND $n = 2$ mice; CD-HFD $n = 3$ mice; CD-HFD/Ticagrelor $n = 3$ mice). All data are shown as mean ± s.e.m. Data in a were analyzed by two-tailed Student's *t* test. Data in **b**, **d**, **e**, **f**, **g** and **j** were analyzed by one way ANOVA with the post hoc Tukey's multiple comparison test. Data in **c** and **h** were analyzed by two way ANOVA with the post hoc Tukey's multiple comparison test. Data in *i* were analyzed by two-tailed Mann–Whitney test, N.s.: not significant $*P < 0.05$. $**P < 0.01$. $***P < 0.001$. $****P < 0.0001$.

Author Manuscript Author Manuscript Author Manuscript Author Manuscript

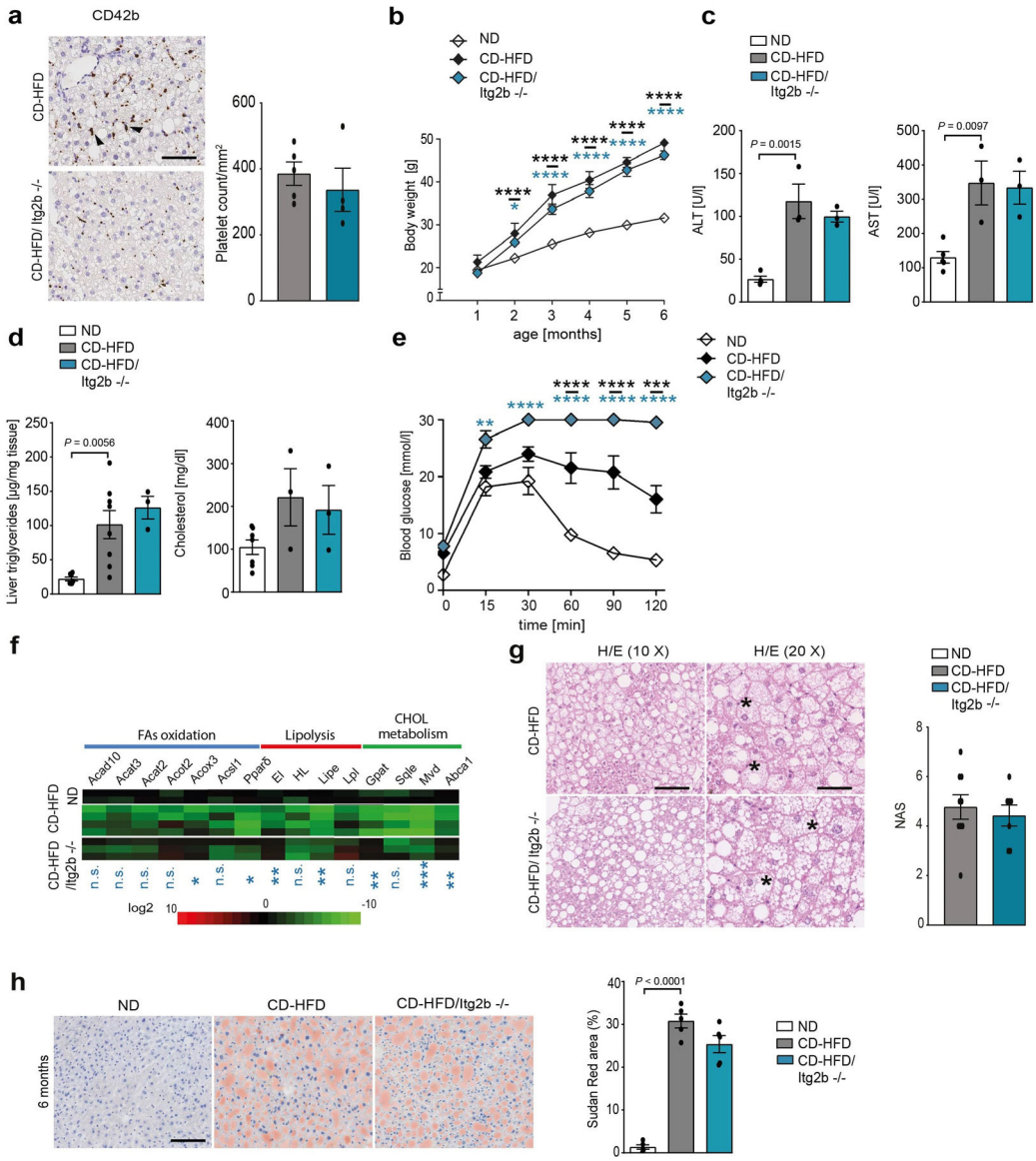

Extended Data Fig. 4 |. Mice with non-functional platelet aggregation are not protected from NASH development.

a, CD42b staining and quantification of 6 months CD-HFD- or CD-HFD/*Itg2b*$^{-/-}$-fed mice (CD-HFD n = 5 mice, CD-HFD/*Itg2b*$^{-/-}$ n = 4 mice). **b**, Body weight development of 6 months CD-HFD or CD-HFD/*Itg2b*$^{-/-}$-fed mice (n = 5/group). Statistics: ND vs CD-HFD (black asterisks), ND vs CD-HFD/*Itg2b*$^{-/-}$ (blue asterisks). **c**, ALT (ND n = 4 mice, CD-HFD n = 3 mice, CD-HFD/*Itg2b*$^{-/-}$ n = 3 mice), AST (ND n = 5 mice, CD-HFD n = 3 mice, CD-HFD/*Itg2b*$^{-/-}$ n = 3 mice), (**d**) liver triglycerides (ND n = 7 mice, CD-HFD n = 8 mice, CD-HFD/*Itg2b*$^{-/-}$ n = 3 mice), and serum cholesterol levels (ND n = 7 mice, CD-HFD n= 3 mice, CD-HFD/*Itg2b*$^{-/-}$ n = 3 mice), (e) IPGTT from mice shown in **a** (n = 3–4 field/mouse, ND n = 4 mice, CD-HFD n= 4 mice, CD-HFD/*Itg2b*$^{-/-}$ n = 10 mice) Statistics: ND vs CD-HFD (black asterisks), ND vs CD-HFD/*Itg2b*$^{-/-}$ (blue asterisks). (**f**) Real-time qPCR analysis for genes involved in lipid metabolism/β-oxidation (ND n = 2 mice, CD-HFD n = 4 mice, CD-HFD/*Itg2b*$^{-/-}$ n = 3 mice). Statistics: CD-HFD vs CD-HFD/*tg2b*$^{-/-}$ (blue

Author Manuscript Author Manuscript Author Manuscript Author Manuscript

asterisks). (**g**) NAS evaluation (CD-HFD $n = 9$ mice, CD-HFD/$tg2b^{-/-}$ $n = 7$ mice) and (**h**) quantification of fat by Sudan red staining of mice shown in **a** ($n = 5$ mice/group), scale bar: 100 μm in 10×, 50 μm in 20×. All data are shown as mean ± s.e.m. Data shown in **a** and **g** were analyzed by two-tailed Student's *t* test. Data in **b**,**e** were analyzed by two-way analysis of variance with the post hoc Bonferroni multiple comparison test. Data in **c**,**d**,**h** were analyzed by one-way analysis of variance with the post hoc Tukey's multiple comparison test. Data in **f** were analyzed by two-tailed Mann-Whitney test; n.s., not significant, $*P < 0.05$, $**P < 0.01$, $***P < 0.001$, $****P < 0.0001$.

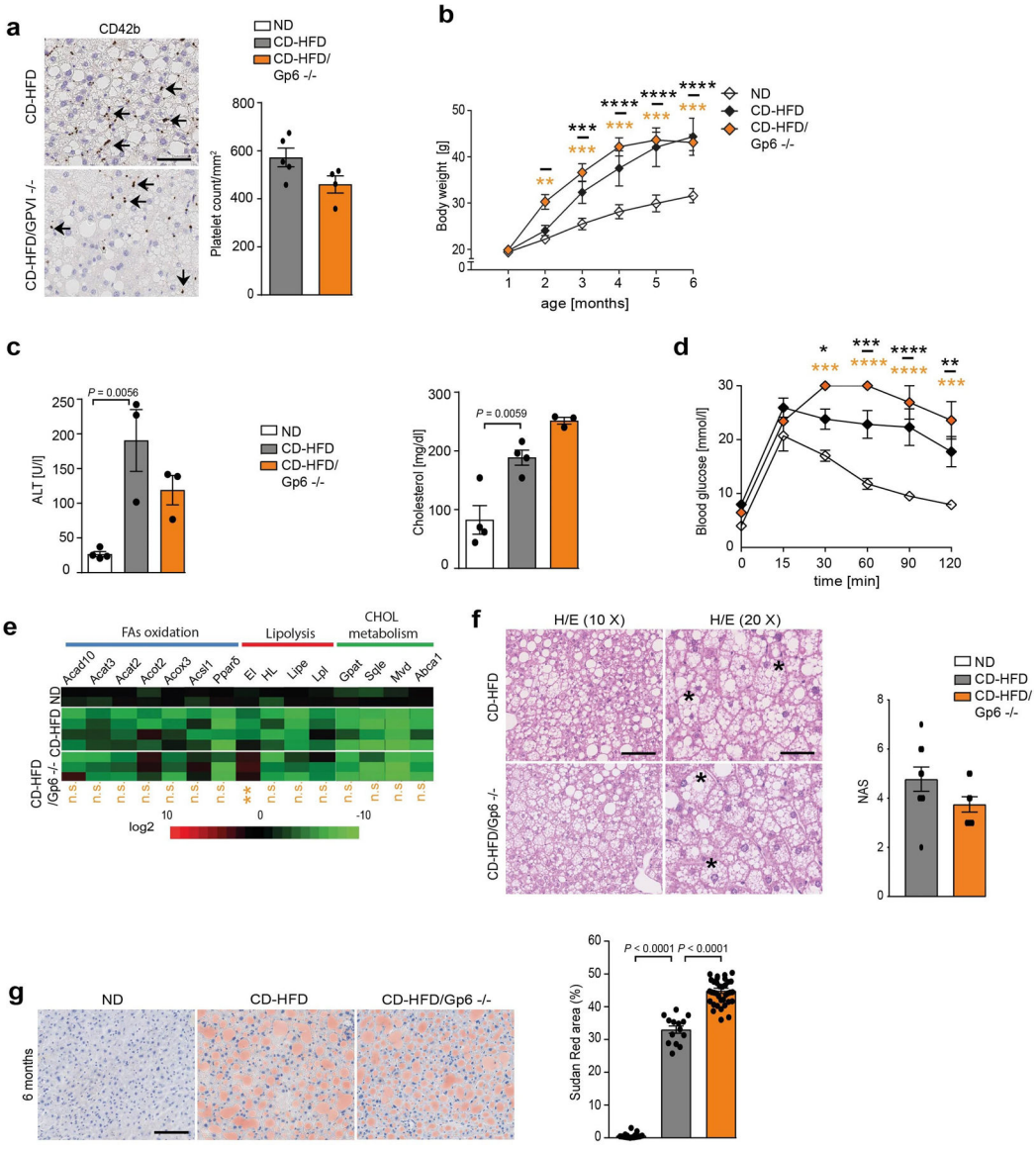

Extended Data Fig. 5 |. Gp6 mice display severe steatosis, NASH and NASH-associated conditions.

a, CD42b staining and quantification of 6 months CD-HFD or CD-HFD/$Gp6^{-/-}$-fed mice (CD-HFD $n = 5$ mice, CD-HFD/$Gp6^{-/-}$ $n = 4$ mice), scale bar: 50 μm. **b**, Body weight ($n = 6$ mice/group), (**c**) ALT, liver triglycerides and cholesterol levels of 6 months mice

Author Manuscript Author Manuscript Author Manuscript Author Manuscript

(ND $n = 4$ mice, CD-HFD $n = 4$ mice, CD-HFD/*Gp6*$^{-/-}$ $n = 3$ mice). Statistics: ND vs CD-HFD (black asterisks), ND vs CD-HFD/*Gp6* (orange asterisks). **d**, IPGTT (ND $n =$ 5 mice, CD-HFD $n = 5$ mice, CD-HFD/*Gp6*$^{-/-}$ $n = 3$ mice). Statistics: ND vs CD-HFD (black asterisks), ND vs CD-HFD/*Gp6*$^{-/-}$ (orange asterisks). **e**, Real-time qPCR analysis for genes involved in lipid metabolism/β-oxidation (ND $n = 2$ mice, CD-HFD $n = 4$ mice, CD-HFD/*Gp6*$^{-/-}$ $n = 3$ mice). **f**, NAS evaluation of mice shown in **a**, damaged hepatocytes are indicated by asterisks (CD-HFD $n = 9$ mice, CD-HFD/*Gp6*$^{-/-}$ $n = 8$ mice), scale bar: 100 μm in 10× and 50 μm in 20×. **g**, Quantification of fat by Sudan red staining in mice shown in **b** ($n = 3$–4 fields/mouse, ND $n = 4$ mice, CD-HFD $n = 4$ mice, CD-HFD/*Gp6*$^{-/-}$ $n = 9$ mice). All data are shown as mean ± s.e.m. Data in **b**,**d** were analyzed by two-way analysis of variance with the post hoc Bonferroni multiple comparison test. Data in **c**,**g** were analyzed by one-way analysis of variance with the post hoc Tukey's multiple comparison test. Data in **e** were analyzed by two-tailed Mann Whitney's test, data in **f** were analyzed by two-tailed Student's *t* test. n.s., not significant, $*P < 0.05$, $**P < 0.01$, $***P < 0.001$, $****P < 0.0001$.

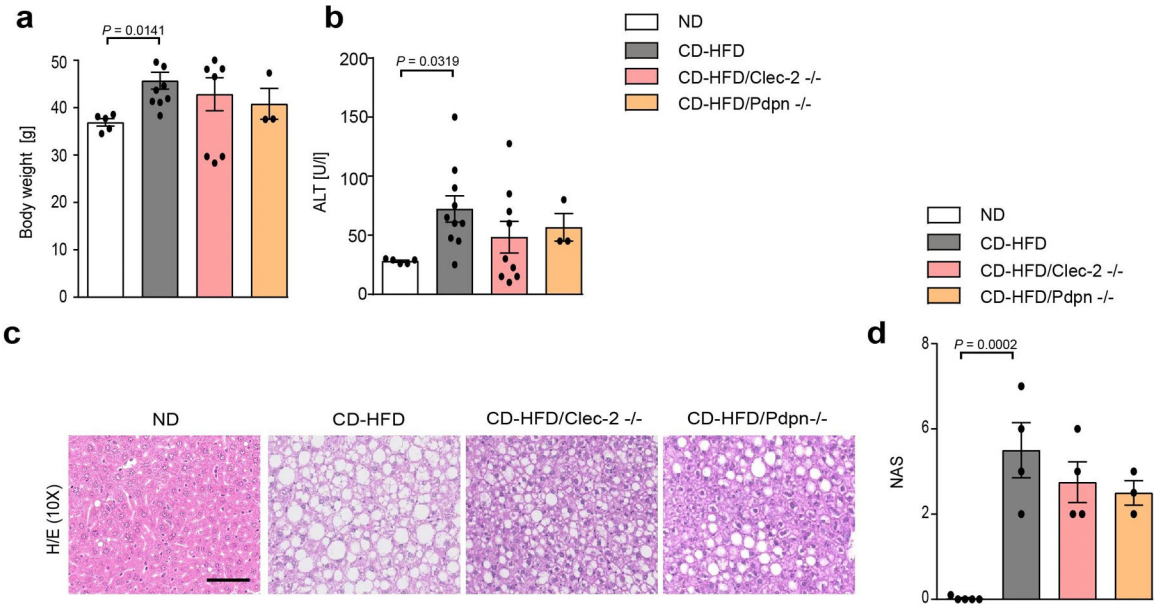

Extended Data Fig. 6 |. Genetic inactivation of Clec-2 or podoplanin does not protect from CD-HFD-induced NASH.

a,**b**, Body weight (**a**) and ALT levels (**b**) (ND $n = 5$ mice, CD-HFD $n = 10$, CD-HFD/*Clec-2* $n = 9$ or CD-HFD/*Pdpn*$^{-/-}$ $n = 3$). (**c**) H&E staining and (**d**) NAS evaluation (ND $n = 5$ mice, CD-HFD $n = 4$, CD-HFD/*Clec-2*$^{-/-}$ $n = 4$ or CD-HFD/*Pdpn*$^{-/-}$ $n = 3$), scale bar: 100 μm. All data are shown as mean ± s.e.m. and analyzed by one-way analysis of variance with the post hoc Tukey's multiple comparison test.

Author Manuscript Author Manuscript Author Manuscript Author Manuscript

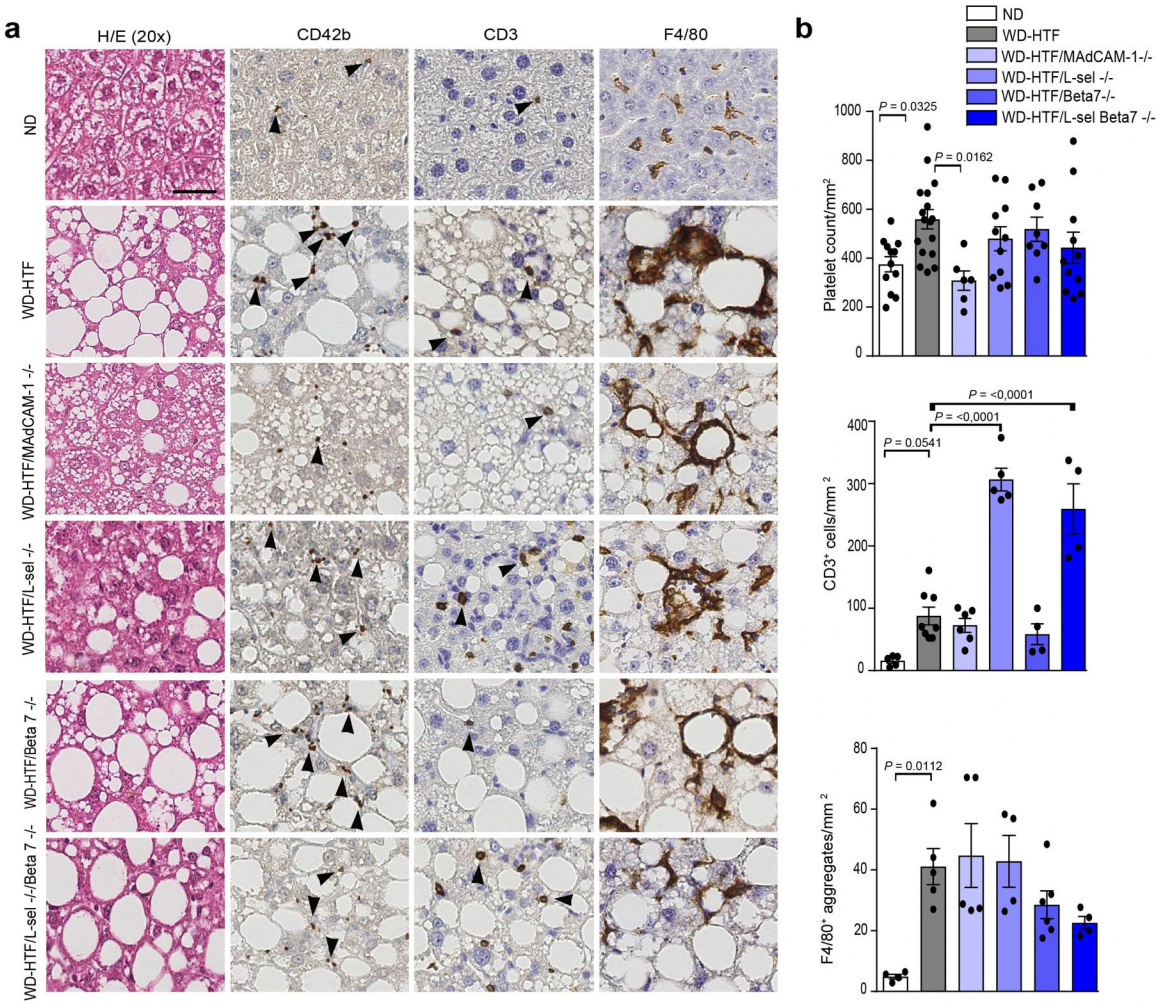

Extended Data Fig. 7 |. MAdCAM-1 has an important role in the platelets recruitment to the liver during NASH development.

a, H&E, CD42b (ND n = 12 mice, WD-HTF n = 17 mice, WD-HTF/*MAdCAM-1*$^{-/-}$ n = 6 mice, WD-HTF/*L-sel*$^{-/-}$ n = 11 mice, WD-HTF/*Beta7*$^{-/-}$ n = 8 mice, WD-HTF/*L-sel*$^{-/-}$/*Beta7*$^{-/-}$ n = 11 mice), CD3 (ND n = 5 mice, WD-HTF n = 8 mice, WD-HTF/*MAdCAM-1*$^{-/-}$ n = 6 mice, WD-HTF/*L-sel*$^{-/-}$ n = 5 mice, WD-HTF/*Beta7*$^{-/-}$ n = 4 mice, WD-HTF/*L-sel*$^{-/-}$*Beta7*$^{-/-}$ n = 4 mice) and F4/80 (ND n = 4 mice, WD-HTF n = 5 mice, WD-HTF/*MAdCAM-1*$^{-/-}$ n = 5 mice, WD-HTF/*-sel*$^{-/-}$ n = 4 mice, WD-HTF/*Beta7*$^{-/-}$ n = 6 mice, WD-HTF/*L-sel*$^{-/-}$/*Beta7*$^{-/-}$ n = 4*MAdCAM-1*$^{-/-}$ mice) stains and (**b**) quantification of IHC of livers of mice mentioned in **a**, scale bar: 50 μm. All data are shown as mean ± s.e.m. Data in **b** were analyzed by one-way analysis of variance with the post hoc Tukey's multiple comparison test.

Author Manuscript Author Manuscript Author Manuscript Author Manuscript

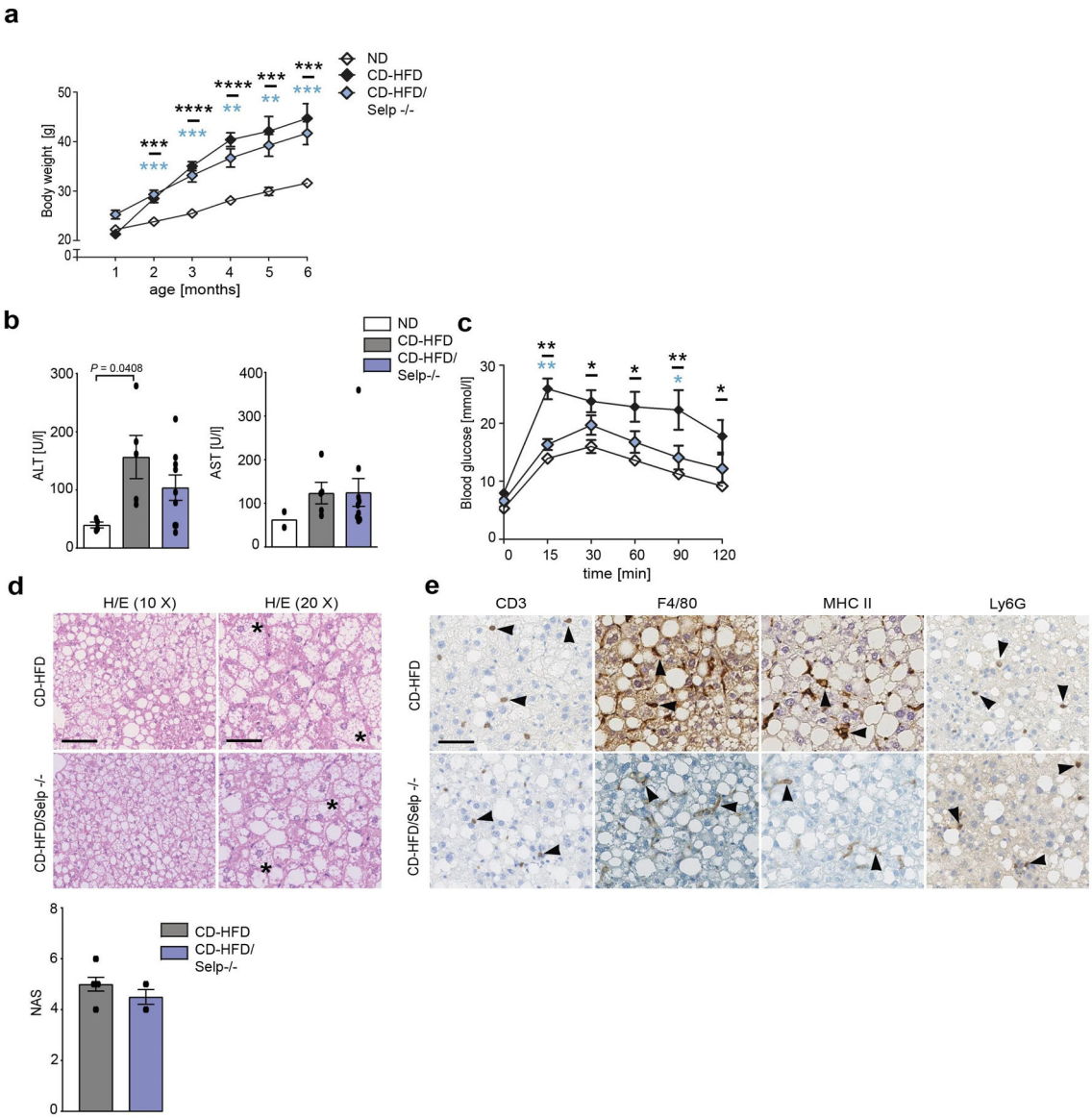

Extended Data Fig. 8 |. Genetic inactivation of P-selectin does not prevent NASH development. **a**,**b**, Body weight development (ND $n = 4$ mice, CD-HFD $n = 3$ mice, CD-HFD/*P-sel*$^{-/-}$ $n = 7$ mice) (**a**) and ALT and AST levels of 6 months ND, CD-HFD or CD-HFD/*P-sel*$^{-/-}$ mice (ND $n = 4$ mice, CD-HFD $n = 5$ mice, CD-HFD/*P-sel* $^{-/-}$ $n = 9$ mice). Statistics: ND vs CD-HFD (black asterisks), ND vs CD-HFD/*P-sel*$^{-/-}$ (violet asterisks). **c**, IPGTT (ND $n = 4$ mice, CD-HFD $n = 5$ mice, CD-HFD/$n = 5$ mice). Statistics: ND vs CD-HFD (black asterisks), CD-HFD vs CD-HFD/*P-sel*$^{-/-}$ (violet asterisks). **d**, NAS evaluation (CD-HFD $n = 8$ mice, CD-HFD/*P-sel*$^{-/-}$ $n = 4$ mice). scale bar: 100 μm in 10×, 50 μm in 20×. **e**, Representative CD3, F4/80, MHCII and Ly6G stainings (CD-HFD $n = 8$ mice, CD-HFD/*P-sel*$^{-/-}$ $n = 4$ mice), scale bar: 50 μm. All data are shown as mean ± s.e.m. Data in **a** and **c** were analyzed by two-way analysis of variance with the post hoc Bonferroni multiple comparison test. Data in **b** were analyzed by one-way analysis of variance with the post hoc Tukey's multiple

comparison test. Data in **d** were analyzed by two-tailed Student's *t* test. n.s., not significant **P* < 0.05, ***P* < 0.01, ****P* < 0.001, *****P* < 0.0001.

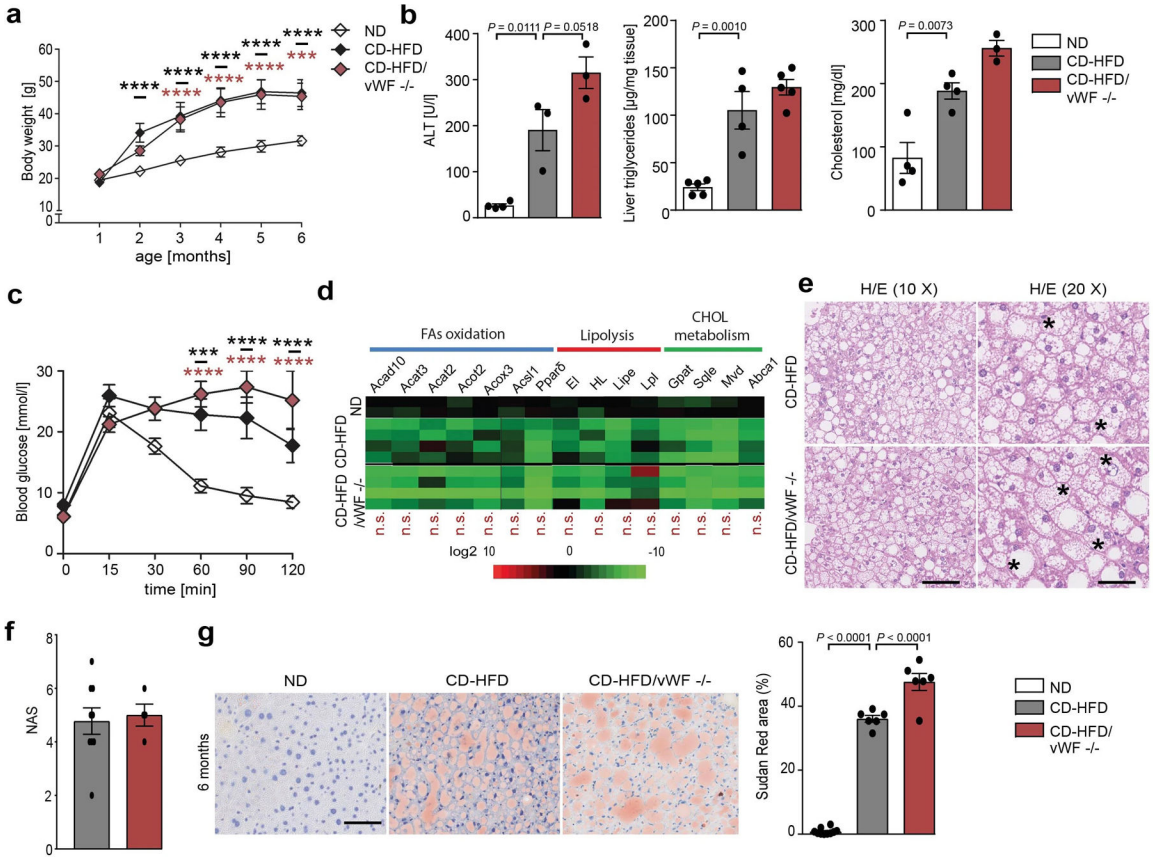

Extended Data Fig. 9 |. vWF$^{-/-}$ mice show steatosis, liver damage and conditions associated with NASH.

a, Body weight development of 6 months ND-, CD-HFD- or CD-HFD/*vWF*-fed mice. Statistics: (*n* = 6 mice/group). Statistics: ND vs CD-HFD (black asterisks), ND vs CD-HFD/*vWF*$^{-/-}$ (red asterisks). **b**, ALT (ND *n* = 4 mice, CD-HFD *n* = 3 mice, CD-HFD/*vWF*$^{-/-}$ *n* = 3 mice), liver triglycerides (ND *n* = 5 mice, CD-HFD *n* = 4 mice, CD-HFD/*vWF*$^{-/-}$ *n* = 5 mice) and serum cholesterol levels (ND *n* = 4 mice, CD-HFD *n* = 4 mice, CD-HFD/*vWF*$^{-/-}$ *n* = 3 mice). **c**, IPGTT (ND *n* = 5 mice, CD-HFD *n* = 5 mice, CD-HFD/*vWF*$^{-/-}$ = 3 mice). Statistics: ND vs CD-HFD (black asterisks), ND vs CD-HFD/*vWF*$^{-/-}$ (red asterisks). **d**, Real-time qPCR analysis for genes involved in lipid metabolism/β-oxidation (ND n = 2 mice, CD-HFD *n* = 4 mice, CD-HFD/*vWF*$^{-/-}$ *n* = 4 mice). **e**, H&E with enlarged hepatocytes (asterisks) and (**f**) evaluation of NAS (CD-HFD *n* = 9 mice, CD-HFD/*vWF*$^{-/-}$ *n* = 4 mice) scale bar: 100 µm in 10X and 50 µm in 20×. **g**, Sudan red staining and quantification of mice shown in **a** (*n* = 2–3 fields/mouse: *n* = 3 mice/group), scale bar: 100 µm. All data are shown as mean ± s.e.m. Data in **a**,**c** were analyzed by two-way analysis of variance with the post hoc Bonferroni multiple comparison test. Data in **b**,**g** were analyzed by one-way analysis of variance with the post hoc Tukey's multiple comparison test. Data in **d** were analyzed by two-tailed Mann-Whitney test. Data in **f** were analyzed by two-tailed Student's *t* test. n.s., not significant, **P* < 0.05, ***P* < 0.01, ****P* < 0.001, *****P* < 0.0001.

Author Manuscript Author Manuscript Author Manuscript Author Manuscript

Author Manuscript Author Manuscript Author Manuscript Author Manuscript

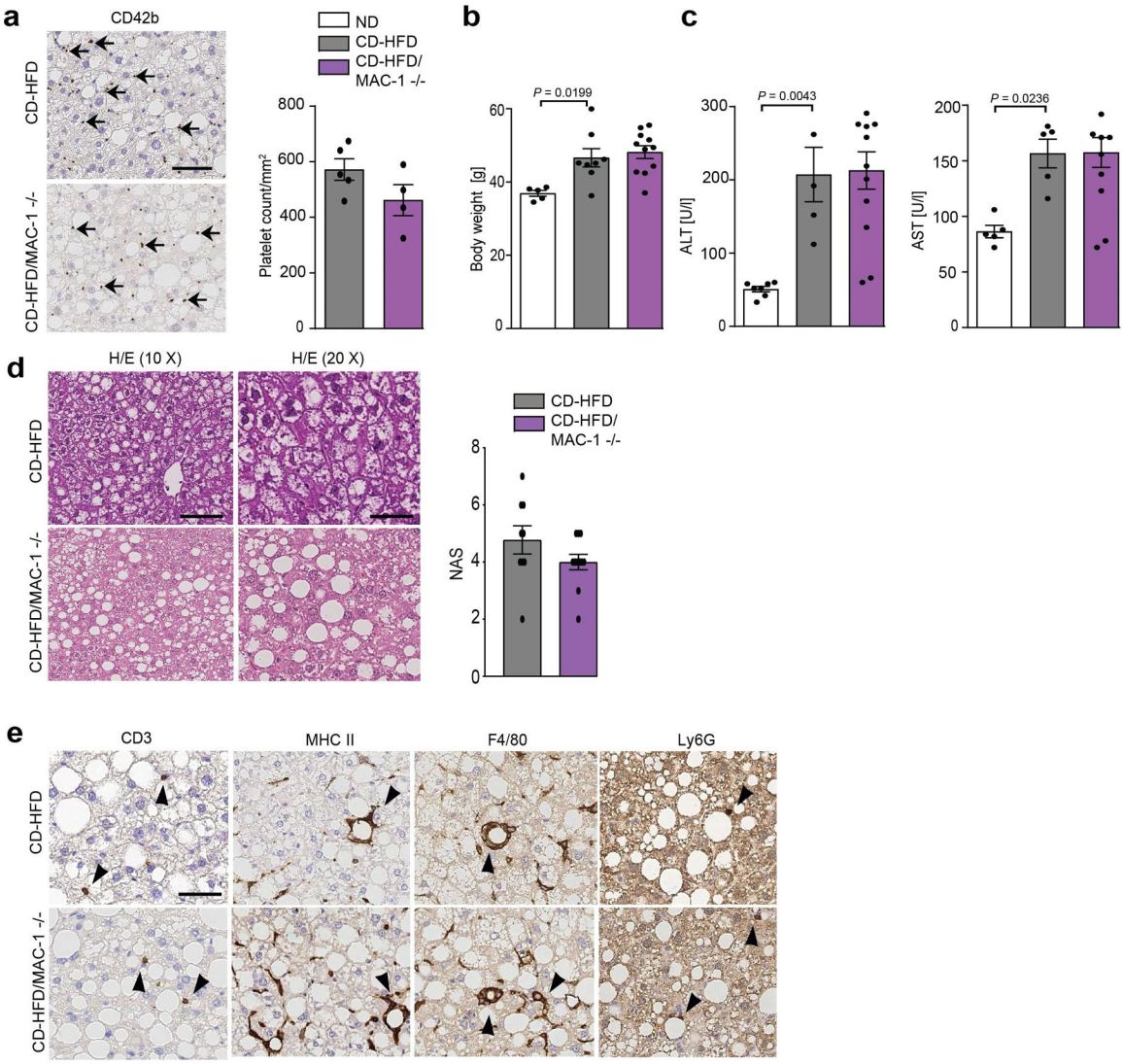

Extended Data Fig. 10 |. Mice lacking Mac-1 show signs of liver injury and develop NASH upon feeding CD-HFD.

a, CD42b staining and quantification of 6 months CD-HFD or CD-HFD/*Mac-1*$^{-/-}$-fed mice (CD-HFD $n = 5$ mice, *Mac-1*/CD-HFD $n = 4$ mice), scale bar: 50 μm (**b**) Body weight (ND $n = 5$ mice, CD-HFD $n = 8$ mice, CD-HFD/*Mac-1*$^{-/-}$ $n = 11$ mice), (**c**) ALT, and AST of 6 months ND, CD-HFD or CD-HFD/*Mac-1*$^{-/-}$-fed mice (CD-HFD $n = 5$ mice, CD-HFD/*Mac-1*$^{-/-}$ $n = 12$ mice) (**d**) NAS evaluation of mice shown in **a** (CD-HFD $n = 9$ mice, CD-HFD/-*Mac-1*$^{-/-}$ $n = 11$ mice) scale bar: 100 μm in 10× and 50 μm in 20×. **e**, Representative CD3^{+}, F4/80^{+}, MHCII^{+} and Ly6G^{+} staining (ND $n = 5$ mice, CD-HFD $n = 8$ mice, CD-HFD/*Mac-1*$^{-/-}$ $n = 11$ mice) and arrows indicate cell/cell aggregates, scale bar: 50 μm. All data are shown as mean ± s.e.m. Data in **a**,**d** were analyzed by two-tailed Student's *t* test. Data in **b**,**c** were analyzed by one-way analysis of variance with the post hoc Tukey's multiple comparison test.

Author Manuscript Author Manuscript Author Manuscript Author Manuscript

Supplementary Material

Refer to Web version on PubMed Central for supplementary material.

Authors

Mohsen Malehmir[1,44], Dominik Pfister[2,44], Suchira Gallage[2,44], Marta Szydlowska[2,44], Donato Inverso[3,4,44], Elena Kotsiliti[2,5], Valentina Leone[2,6], Moritz Peiseler[7,8], Bas G. J. Surewaard[8,9,10], Dominik Rath[11], Adnan Ali[2], Monika Julia Wolf[1], Hannah Drescher[12], Marc E. Healy[1], Daniel Dauch[13,14], Daniela Kroy[12], Oliver Krenkel[12], Marlene Kohlhepp[12], Thomas Engleitner[15,16,17], Alexander Olkus[2,18], Tjeerd Sijmonsma[2], Julia Volz[19], Carsten Deppermann[19], David Stegner[19], Patrick Helbling[20], César Nombela-Arrieta[20], Anahita Rafiei[20], Martina Hinterleitner[13,14], Marcel Rall[11], Florian Baku[11], Oliver Borst[11], Caroline L. Wilson[21], Jack Leslie[21], Tracy O'Connor[5,22], Christopher J. Weston[23], Abhishek Chauhan[23], David H. Adams[23,24], Lozan Sheriff[25], Ana Teijeiro[26], Marco Prinz[27,28,29], Ruzhica Bogeska[30,31], Natasha Anstee[30,31], Malte N. Bongers[32], Mike Notohamiprodjo[32], Tobias Geisler[33], Dominic J. Withers[34,35], Jerry Ware[36], Derek A. Mann[21], Hellmut G. Augustin[3,4], Alexandros Vegiopoulos[37], Michael D. Milsom[30,31], Adam J. Rose[38], Patricia F. Lalor[23], Josep M. Llovet[39,40,41], Roser Pinyol[40], Frank Tacke[12], Roland Rad[15,16,17], Matthias Matter[42], Nabil Djouder[26], Paul Kubes[7,8,9], Percy A. Knolle[22], Kristian Unger[6], Lars Zender[13,14,43], Bernhard Nieswandt[19], Meinrad Gawaz[11], Achim Weber[1,45,*], Mathias Heikenwalder[2,5,45,*]

Affiliations

[1]Department of Pathology and Molecular Pathology, University and University Hospital Zurich, Zurich, Switzerland.

[2]Division of Chronic Inflammation and Cancer, German Cancer Research Center Heidelberg (DKFZ), Heidelberg, Germany.

[3]Division of Vascular Oncology and Metastasis, German Cancer Research Center Heidelberg (DKFZ-ZMBH Alliance), Heidelberg, Germany.

[4]European Center of Angioscience (ECAS), Medical Faculty Mannheim, Heidelberg University, Mannheim, Germany.

[5]Institute for Virology, Technische Universität München/Helmholtz Zentrum München, Munich, Germany.

[6]Research Unit of Radiation Cytogenetics, Helmholtz Zentrum München, Neuherberg, Germany.

[7]Calvin Phoebe & Joan Snyder Institute for Chronic Diseases, Cumming School of Medicine, University of Calgary, Calgary, Alberta, Canada.

[8]Department of Physiology and Pharmacology, Cumming School of Medicine, University of Calgary, Calgary, Alberta, Canada.

Author Manuscript Author Manuscript Author Manuscript Author Manuscript

[9]Department of Microbiology, Immunology & Infectious Diseases, Cumming School of Medicine, University of Calgary, Calgary, Alberta, Canada.

[10]Department of Medical Microbiology, University Medical Center, Utrmeecht, the Netherlands.

[11]Department of Cardiology and Circulatory Diseases, Internal Medicine Clinic III, Eberhard Karls University Tübingen, Tübingen, Germany.

[12]Department of Medicine III, University Hospital RWTH Aachen, Aachen, Germany.

[13]Department of Internal Medicine VIII, University Hospital Tübingen, Tübingen, Germany.

[14]Department of Physiology I, Institute of Physiology, Eberhard Karls University Tübingen, Tübingen, Germany.

[15]Center for Translational Cancer Research (TranslaTUM), Technische Universität München, Munich, Germany.

[16]Department of Medicine II, Klinikum Rechts der Isar, Technische Universität München, Munich, Germany.

[17]German Cancer Consortium (DKTK), German Cancer Research Center (DKFZ), Heidelberg, Germany.

[18]Medical Faculty, University of Heidelberg, Heidelberg, Germany.

[19]Institute of Experimental Biomedicine, University Hospital and Rudolf Virchow Center, University of Würzburg, Würzburg, Germany.

[20]Hematology, University Hospital and University of Zurich, Zurich, Switzerland.

[21]Newcastle Fibrosis Research Group, Institute of Cellular Medicine, Newcastle University, Newcastle Upon Tyne, UK.

[22]Institute of Molecular Immunology and Experimental Oncology, Technical University of Munich, Munich, Germany.

[23]Centre for Liver Research and National Institute for Health Research (NIHR) Birmingham Liver Biomedical Research Unit, Birmingham, UK.

[24]Liver Unit, University Hospitals Birmingham NHS Trust, Birmingham, UK.

[25]Institute for Cardiovascular Sciences, University of Birmingham, Birmingham, UK.

[26]Cancer Cell Biology Programme, Growth Factors, Nutrients and Cancer Group, Spanish National Cancer Research Centre, CNIO, Madrid, Spain.

[27]Institute of Neuropathology, Medical Faculty, University of Freiburg, Freiburg, Germany.

[28]Signalling Research Centres BIOSS and CIBSS, University of Freiburg, Freiburg, Germany.

Author Manuscript Author Manuscript Author Manuscript Author Manuscript

[29]Center for NeuroModulation, Faculty of Medicine, University of Freiburg, Freiburg, Germany.

[30]Division of Experimental Hematology, Deutsches Krebsforschungszentrum (DKFZ), Heidelberg, Germany.

[31]DKFZ-ZMBH Alliance, Heidelberg Institute for Stem Cell Technology and Experimental Medicine (HI-STEM gGmbH) Deutsches Krebsforschungszentrum (DKFZ), Heidelberg, Germany.

[32]Department of Diagnostic and Interventional Radiology, University Hospital of Tübingen, Tübingen, Germany.

[33]Department of Cardiovascular Medicine, University Hospital, Eberhard Karls University of Tübingen, Tübingen, Germany.

[34]Metabolic Signalling Group, MRC London Institute of Medical Sciences, London, UK.

[35]Institute of Clinical Sciences, Faculty of Medicine, Imperial College London, London, UK.

[36]Department of Physiology and Biophysics, University of Arkansas for Medical Sciences, Little Rock, AR, USA.

[37]DKFZ Junior Group Metabolism and Stem Cell Plasticity, German Cancer Research Center (DKFZ), Heidelberg, Germany.

[38]Nutrient Metabolism and Signalling Lab, Department of Biochemistry and Molecular Biology, School of Biomedical Sciences, and Metabolism, Diabetes and Obesity Program, Biomedicine Discovery Institute, Monash University, Clayton, Australia.

[39]Mount Sinai Liver Cancer Program (Divisions of Liver Diseases, Department of Medicine, Department of Pathology, Recanati Miller Transplantation Institute), Tisch Cancer Institute, Icahn School of Medicine at Mount Sinai, New York, NY, USA.

[40]Liver Cancer Translational Research Laboratory, IDIBAPS, Liver Unit, Hospital Clinic, University of Barcelona, Barcelona, Catalonia, Spain.

[41]Institució Catalana de Recerca i Estudis Avançats (ICREA), Barcelona, Catalonia, Spain.

[42]Institute of Pathology, University Hospital of Basel, Basel, Switzerland.

[43]Translational Gastrointestinal Oncology Group, German Consortium for Translational Cancer Research (DKTK), German Cancer Research Center (DKFZ), Heidelberg, Germany.

[44]These authors contributed equally: Mohsen Malehmir, Dominik Pfister, Suchira Gallage, Marta Szydlowska, Donato Inverso.

[45]These authors jointly supervised this work: Achim Weber, Mathias Heikenwalder.

Author Manuscript Author Manuscript Author Manuscript Author Manuscript

Acknowledgements

We thank D. Heide, J. Hetzer, R. Hillermann, C. Gropp, F. Müller, S. Prokosch, D. Kull, R. Dunkl, O. Seelbach, M. Bawohl, R. Maire, M. Bieri, C. Mittmann, H. Honcharova-Biletska, A. Fitsche, A. Adili, P. Münzer, T. Nussbaumer, F. Prutek, G. Dharmalingam and I. Singh for excellent technical assistance. We thank K. Nikolaou for the help with the human cohort recruitment and analysis. M. Malehmir was partially supported by grants from the University Zurich (Zurich Integrative Human Physiology (ZHIP) Sprint Fellowship) and from the Hartmann Müller Stiftung, Zurich. A.W. was supported by a grant from the Swiss National Science Foundation (320030_182764/1). M. Heikenwaelder was supported by an ERC Consolidator grant (HepatoMetaboPath), an EOS grant, SFBTR 209, SFBTR179, Research Foundation Flanders (FWO) under grant 30826052 (EOS Convention MODEL-IDI), Deutsche Krebshilfe projects 70113166 and 70113167, and the Helmholtz-Gemeinschaft, Zukunftsthema 'Immunology and Inflammation' (ZT-0027). This project has received funding from the European Union's Horizon 2020 research and innovation program under grant agreement 667273 and the DFG (SFB/TR 240 (project 374031971) to B.N. and D.S.), ERC Consolidator grant 'CholangioConcept' (to L.Z.), and the German Research Foundation (DFG): grants FOR2314, SFB685 and the Gottfried Wilhelm Leibniz Program (to L.Z.). Further funding was provided by the German Ministry for Education and Research (BMBF) (eMed/Multiscale HCC), the German Universities Excellence Initiative (third funding line: 'future concept'), the German Center for Translational Cancer Research (DKTK) and the German-Israeli Cooperation in Cancer Research (DKFZ-MOST) (to L.Z. and M. Heikenwaelder). D.I. was supported by an EMBO Long-term Fellowship. J.M.L. is supported by Asociación Española Contra el Cáncer (Accelerator award: HUNTER), Spanish National Health Institute (SAF2013-41027), Generalitat de Catalunya (SGR 1162 and AGAUR, SGR-1358), the Samuel Waxman Cancer Research Foundation, the US Department of Defense (CA150272P3), the European Commission Horizon 2020 Program (HEPCAR, proposal number 667273-2), and the National Cancer Institute (P30 CA196521). D.A.M. is supported by CRUK grant C18342/A23390 and MRC grant MR/K001949/1. M.P. is supported by the German Research Foundation (DFG). M.G., T.G. and D.R. was supported by grants from the German Research Foundation (KFO274 and SFB/TR240 (project 374031971)). D.J.W. received a Wellcome Trust Strategic Award (098565/Z/12/Z) and funding from the Medical Research Council (MC-A654-5QB40). C.L.W. was funded by CRUK project Cancer Research UK Programme Grant C18342/A23390. H.G.A. has been supported by the Deutsche Forschungsgemeinschaft (SFB-TR209 'Liver Cancer').

Data availability

Data that support the findings of this study have been uploaded to ArrayExpress (www.ebi.ac.uk/arrayexpress/) and the data set is available under the accession number E-MTAB-6073, entitled 'Transcriptomic differences in livers of mice fed with normal diet and choline-deficient high-fat diet'.

References

1. Fleet SE, Lefhowitch JH & Lavine JE Current concepts in pediatric nonalcoholic fatty liver disease. Gastroenterol. Clin. North Am 46, 217–231 (2017). [PubMed: 28506362]
2. European Association for the Study of the Liver, European Association for the Study of Diabetes & European Association for the Study of Obesity. EASL-EASD-EASO Clinical Practice Guidelines for the management of non-alcoholic fatty liver disease. J. Hepatol 64, 1388–1402 (2016). [PubMed: 27062661]
3. Younossi Z et al. Global perspectives on non-alcoholic fatty liver disease and non-alcoholic steatohepatitis. Hepatology 10.1002/hep.30251 (2018).
4. Brunt EM et al. Nonalcoholic fatty liver disease. Nat. Rev. Dis. Primers 1, 15080 (2015). [PubMed: 27188459]
5. Friedman SL, Neuschwander-Tetri BA, Rinella M & Sanyal AJ Mechanisms of NAFLD development and therapeutic strategies. Nat. Med 24, 908–922 (2018). [PubMed: 29967350]
6. El-Serag HB & Kanwal F Epidemiology of hepatocellular carcinoma in the United States: where are we? Where do we go? Hepatology 60, 1767–1775 (2014). [PubMed: 24839253]
7. Torre LA et al. Global cancer statistics, 2012. CA Cancer J. Clin 65, 87–108 (2015). [PubMed: 25651787]
8. Ozakyol A Global epidemiology of hepatocellular carcinoma (HCC epidemiology). J. Gastrointest. Cancer 48, 238–240 (2017). [PubMed: 28626852]

Author Manuscript Author Manuscript Author Manuscript Author Manuscript

9. Ashfin A et al. Health effects of overweight and obesity in 195 countries over 25 years. N. Engl. J. Med 377, 13–27 (2017). [PubMed: 28604169]
10. Ringelhan M, Pfister D, O'Connor T, Pikarsky E & Heikenwalder M The immunology of hepatocellular carcinoma. Nat. Immunol 19, 222–232 (2018). [PubMed: 29379119]
11. Wolf MJ et al. Metabolic activation of intrahepatic CD8+ T cells and NKT cells causes nonalcoholic steatohepatitis and liver cancer via cross-talk with hepatocytes. Cancer Cell. 26, 549–564 (2014). [PubMed: 25314080]
12. Michelson AD How platelets work: platelet function and dysfunction. J. Thromb. Thrombolysis 16, 7–12 (2003). [PubMed: 14760205]
13. Chauhan A, Adams DH, Watson SP & Lalor PF Platelets: no longer bystanders in liver disease. Hepatology 64, 1774–1784 (2016). [PubMed: 26934463]
14. Gawaz M, Langer H & May AE Platelets in inflammation and atherogenesis. J. Clin. Invest 115, 3378–3384 (2005). [PubMed: 16322783]
15. Jackson SP Arterial thrombosis—insidious, unpredictable and deadly. Nat. Med 17, 1423–1436 (2011). [PubMed: 22064432]
16. Fujita K et al. Effectiveness of antiplatelet drugs against experimental non-alcoholic fatty liver disease. Gut 57, 1583–1591 (2008). [PubMed: 18596193]
17. Lang PA et al. Aggravation of viral hepatitis by platelet-derived serotonin. Nat. Med 14, 756–761 (2008). [PubMed: 18516052]
18. Iannacone M et al. Platelets mediate cytotoxic T lymphocyte-induced liver damage. Nat. Med 11, 1167–1169 (2005). [PubMed: 16258538]
19. Iannacone M, Sitia G, Narvaiza I, Ruggeri ZM & Guidotti LG Antiplatelet drug therapy moderates immune-mediated liver disease and inhibits viral clearance in mice infected with a replication-deficient adenovirus. Clin. Vaccine Immunol 14, 1532–1535 (2007). [PubMed: 17881509]
20. Sitia G et al. Antiplatelet therapy prevents hepatocellular carcinoma and improves survival in a mouse model of chronic hepatitis B. Proc. Natl Acad. Sci. USA 109, E2165–E2172 (2012). [PubMed: 22753481]
21. Shen H, Shahzad G, Jawairia M, Bostick RM & Mustacchia P Association between aspirin use and the prevalence of nonalcoholic fatty liver disease: a cross-sectional study from the third national health and nutrition examination survey. Aliment. Pharmacol. Ther 40, 1066–1073 (2014). [PubMed: 25176122]
22. Musso G, Cassader M, Rosina F & Gambino R Impact of current treatments on liver disease, glucose metabolism and cardiovascular risk in non-alcoholic fatty liver disease (NAFLD): a systematic review and meta-analysis of randomised trials. Diabetologia 55, 885–904 (2012). [PubMed: 22278337]
23. Wong VW et al. Pathogenesis and novel treatment options for non-alcoholic steatohepatitis. Lancet Gastroenterol. Hepatol 1, 56–67 (2016). [PubMed: 28404113]
24. Clapper JR et al. Diet-induced mouse model of fatty liver disease and nonalcoholic steatohepatitis reflecting clinical disease progression and methods of assessment. Am. J. Physiol. Gastrointest. Liver Physiol 305, G483–G495 (2013). [PubMed: 23886860]
25. Wang B et al. Intestinal phospholipid remodeling is required for dietary-lipid uptake and survival on a high-fat diet. Cell. Metab 23, 492–504 (2016). [PubMed: 26833026]
26. Weston CJ et al. Vascular adhesion protein-1 promotes liver inflammation and drives hepatic fibrosis. J. Clin. Invest 125, 501–520 (2015). [PubMed: 25562318]
27. Gomes AL et al. Metabolic inflammation-associated il-17a causes non-alcoholic steatohepatitis and hepatocellular carcinoma. Cancer Cell. 30, 161–175 (2016). [PubMed: 27411590]
28. Angulo P et al. Liver fibrosis, but no other histologic features, is associated with long-term outcomes of patients with nonalcoholic fatty liver disease. Gastroenterology 149, 389–397 e310 (2015). [PubMed: 25935633]
29. Dulai PS et al. Increased risk of mortality by fibrosis stage in nonalcoholic fatty liver disease: Systematic review and meta-analysis. Hepatology 65, 1557–1565 (2017). [PubMed: 28130788]
30. Bayindir-Buchhalter I et al. Cited4 is a sex-biased mediator of the antidiabetic glitazone response in adipocyte progenitors. EMBO Mol. Med 10, e8613 (2018). [PubMed: 29973382]

Author Manuscript Author Manuscript Author Manuscript Author Manuscript

31. Mauri L et al. Twelve or 30 months of dual antiplatelet therapy after drug-eluting stents. N. Engl. J. Med 371, 2155–2166 (2014). [PubMed: 25399658]
32. He G & Karin M NF-kappaB and STAT3—key players in liver inflammation and cancer. Cell Res 21, 159–168 (2011). [PubMed: 21187858]
33. Kral JB, Schrottmaier WC, Salzmann M & Assinger A Platelet interaction with innate immune cells. Transfus. Med. Hemother 43, 78–88 (2016). [PubMed: 27226790]
34. Husted S & van Giezen JJ Ticagrelor: the first reversibly binding oral P2Y12 receptor antagonist. Cardiovasc. Ther 27, 259–274 (2009). [PubMed: 19604248]
35. Wallentin L et al. Ticagrelor versus clopidogrel in patients with acute coronary syndromes. N. Engl. J. Med 361, 1045–1057 (2009). [PubMed: 19717846]
36. Deppermann C et al. Gray platelet syndrome and defective thrombo-inflammation in *Nbeal2*-deficient mice. J. Clin. Invest 123, 3331–3342 (2013). [PubMed: 23863626]
37. Albers CA et al. Exome sequencing identifies NBEAL2 as the causative gene for gray platelet syndrome. Nat. Genet 43, 735–737 (2011). [PubMed: 21765411]
38. Kahr WH et al. Mutations in NBEAL2, encoding a BEACH protein, cause gray platelet syndrome. Nat. Genet 43, 738–740 (2011). [PubMed: 21765413]
39. Gunay-Aygun M et al. NBEAL2 is mutated in gray platelet syndrome and is required for biogenesis of platelet alpha-granules. Nat. Genet 43, 732–734 (2011). [PubMed: 21765412]
40. Kopec AK et al. Thrombin promotes diet-induced obesity through fibrin-driven inflammation. J. Clin. Invest 127, 3152–3166 (2017). [PubMed: 28737512]
41. Jandrot-Perrus M et al. Cloning, characterization, and functional studies of human and mouse glycoprotein VI: a platelet-specific collagen receptor from the immunoglobulin superfamily. Blood 96, 1798–1807 (2000). [PubMed: 10961879]
42. Drescher HK et al. beta7-Integrin and MAdCAM-1 play opposing roles during the development of non-alcoholic steatohepatitis. J. Hepatol 66, 1251–1264 (2017). [PubMed: 28192190]
43. Haemmerle M, Stone RL, Menter DG, Afshar-Kharghan V & Sood AK The platelet lifeline to cancer: challenges and opportunities. Cancer Cell. 33, 965–983 (2018). [PubMed: 29657130]
44. Kleinschnitz C et al. Targeting platelets in acute experimental stroke: impact of glycoprotein Ib, VI, and IIb/IIIa blockade on infarct size, functional outcome, and intracranial bleeding. Circulation 115, 2323–2330 (2007). [PubMed: 17438148]
45. Kanaji T, Russell S & Ware J Amelioration of the macrothrombocytopenia associated with the murine Bernard-Soulier syndrome. Blood 100, 2102–2107 (2002). [PubMed: 12200373]
46. Subramaniam M et al. Defects in hemostasis in P-selectin-deficient mice. Blood 87, 1238–1242 (1996). [PubMed: 8608210]
47. Blenner MA, Dong X & Springer TA Structural basis of regulation of von Willebrand factor binding to glycoprotein Ib. J. Biol. Chem 289, 5565–5579 (2014). [PubMed: 24391089]
48. Wang Y et al. Leukocyte integrin Mac-1 regulates thrombosis via interaction with platelet GPIbalpha. Nat. Commun 8, 15559 (2017). [PubMed: 28555620]
49. George JN Platelets. Lancet 355, 1531–1539 (2000). [PubMed: 10801186]
50. Langer HF et al. Platelets contribute to the pathogenesis of experimental autoimmune encephalomyelitis. Circ. Res 110, 1202–1210 (2012). [PubMed: 22456181]
51. Romo GM et al. The glycoprotein Ib-IX-V complex is a platelet counterreceptor for P-selectin. J. Exp. Med 190, 803–814 (1999). [PubMed: 10499919]
52. Kroll MH, Harris TS, Moake JL, Handin RI & Schafer AI von Willebrand factor binding to platelet GpIb initiates signals for platelet activation. J. Clin. Invest 88, 1568–1573 (1991). [PubMed: 1939645]
53. Wong J et al. A minimal role for selectins in the recruitment of leukocytes into the inflamed liver microvasculature. J. Clin. Invest 99, 2782–2790 (1997). [PubMed: 9169509]
54. Dutting S et al. A Cdc42/RhoA regulatory circuit downstream of glycoprotein Ib guides transendothelial platelet biogenesis. Nat. Commun 8, 15838 (2017). [PubMed: 28643773]
55. Min HK et al. Increased hepatic synthesis and dysregulation of cholesterol metabolism is associated with the severity of nonalcoholic fatty liver disease. Cell Metab 15, 665–674 (2012). [PubMed: 22560219]

Author Manuscript Author Manuscript Author Manuscript Author Manuscript

56. Townsend SA & Newsome PN Non-alcoholic fatty liver disease in 2016. Br. Med. Bull 119, 143–156 (2016). [PubMed: 27543499]
57. Neuschwander-Tetri BA et al. Farnesoid X nuclear receptor ligand obeticholic acid for non-cirrhotic, non-alcoholic steatohepatitis (FLINT): a multicentre, randomised, placebo-controlled trial. Lancet 385, 956–965 (2015). [PubMed: 25468160]
58. Boege Y et al. A dual role of caspase-8 in triggering and sensing proliferation-associated dna damage, a key determinant of liver cancer development. Cancer Cell. 32, 342–359 e310 (2017). [PubMed: 28898696]
59. Franchi F, Rollini F & Angiolillo DJ Antithrombotic therapy for patients with STEMI undergoing primary PCI. Nat. Rev. Cardiol 14, 361–379 (2017). [PubMed: 28230176]
60. Margetts J et al. Neutrophils: driving progression and poor prognosis in hepatocellular carcinoma? Br. J. Cancer 118, 248–257 (2018). [PubMed: 29123264]
61. Bender M, Hagedorn I & Nieswandt B Genetic and antibody-induced glycoprotein VI deficiency equally protects mice from mechanically and $FeCl_3$-induced thrombosis. J. Thromb. Haemost 9, 1423–1426 (2011). [PubMed: 21535392]
62. Tiedt R, Schomber T, Hao-Shen H & Skoda RC Pf4-Cre transgenic mice allow the generation of lineage-restricted gene knockouts for studying megakaryocyte and platelet function in vivo. Blood 109, 1503–1506 (2007). [PubMed: 17032923]
63. World Medical Association Declaration of Helsinki. Recommendations guiding physicians in biomedical research involving human subjects. Cardiovasc. Res 35, 2–3 (1997). [PubMed: 9302340]
64. International Conference on Harmonisation of Technical Requirements for Registration of Pharmaceuticals for Human Use. ICH harmonized tripartite guideline: guideline for good clinical practice. J. Postgrad. Med 47, 45–50 (2001). [PubMed: 11590294]
65. European Commission. Directive 2001/20/EC of the European Parliament and of the Council of 4 April 2001 on the approximation of the laws, regulations and administrative provisions of the member states relating to the implementation of good clinical practice in the conduct of clinical trials on medicinal products for human use. Med Etika Bioet 9, 12–19 (2002). [PubMed: 16276663]
66. Grundy SM et al. Implications of recent clinical trials for the national cholesterol education program adult treatment panel III guidelines. Circulation 110, 227–239 (2004). [PubMed: 15249516]
67. Werner M et al. All-In-One: advanced preparation of human parenchymal and non-parenchymal liver cells. PLoS One 10, e0138655 (2015). [PubMed: 26407160]
68. Maaten L. J. Pvd & Hinton GE. Visualizing high-dimensional data using t-SNE. J Mach Learn Res 9, 2579–2605 (2008).
69. Raasch J et al. IkappaB kinase 2 determines oligodendrocyte loss by non-cell-autonomous activation of NF-kappaB in the central nervous system. Brain 134, 1184–1198 (2011). [PubMed: 21310728]
70. Bergmeier W et al. Flow cytometric detection of activated mouse integrin alphaIIbbeta3 with a novel monoclonal antibody. Cytometry 48, 80–86 (2002). [PubMed: 12116368]
71. Schulte V et al. Targeting of the collagen-binding site on glycoprotein VI is not essential for in vivo depletion of the receptor. Blood 101, 3948–3952 (2003). [PubMed: 12531795]
72. Nieswandt B et al. Long-term antithrombotic protection by in vivo depletion of platelet glycoprotein VI in mice. J. Exp. Med 193, 459–469 (2001). [PubMed: 11181698]
73. Gruner S et al. Multiple integrin-ligand interactions synergize in shear-resistant platelet adhesion at sites of arterial injury in vivo. Blood 102, 4021–4027 (2003). [PubMed: 12893753]
74. Nieswandt B, Bergmeier W, Rackebrandt K, Gessner JE & Zirngibl H Identification of critical antigen-specific mechanisms in the development of immune thrombocytopenic purpura in mice. Blood 96, 2520–2527 (2000). [PubMed: 11001906]
75. May F et al. CLEC-2 is an essential platelet-activating receptor in hemostasis and thrombosis. Blood 114, 3464–3472 (2009). [PubMed: 19641185]

Author Manuscript Author Manuscript Author Manuscript Author Manuscript

76. Subramanian A et al. Gene set enrichment analysis: a knowledge-based approach for interpreting genome-wide expression profiles. Proc. Natl Acad. Sci. USA 102, 15545–15550 (2005). [PubMed: 16199517]
77. Parekh S, Ziegenhain C, Vieth B, Enard W & Hellmann I The impact of amplification on differential expression analyses by RNA-seq. Sci. Rep 6, 25533 (2016). [PubMed: 27156886]
78. Macosko EZ et al. Highly parallel genome-wide expression profiling of individual cells using nanoliter droplets. Cell 161, 1202–1214 (2015). [PubMed: 26000488]
79. Love MI, Huber W & Anders S Moderated estimation of fold change and dispersion for RNA-seq data with DESeq2. Genome Biol 15, 550 (2014). [PubMed: 25516281]
80. Kuleshov MV et al. Enrichr: a comprehensive gene set enrichment analysis web server 2016 update. Nucleic Acids Res 44, W90–W97 (2016). [PubMed: 27141961]
81. Levin YS et al. Effect of echo-sampling strategy on the accuracy of out-of-phase and in-phase multiecho gradient-echo MRI hepatic fat fraction estimation. J. Magn. Reson. Imaging 39, 567–575 (2014). [PubMed: 23720420]
82. Merkle EM & Nelson RC Dual gradient-echo in-phase and opposed-phase hepatic MR imaging: a useful tool for evaluating more than fatty infiltration or fatty sparing. Radiographics 26, 1409–1418 (2006). [PubMed: 16973772]
83. Nombela-Arrieta C et al. Quantitative imaging of haematopoietic stem and progenitor cell localization and hypoxic status in the bone marrow microenvironment. Nat. Cell Biol 15, 533–543 (2013). [PubMed: 23624405]
84. Thon JN & Italiano JE Platelets: production, morphology and ultrastructure. Handb. Exp. Pharmacol 210, 3–22 (2012).
85. Thon JN & Italiano JE Jr. Does size matter in platelet production? Blood 120, 1552–1561 (2012). [PubMed: 22665937]

Author Manuscript Author Manuscript Author Manuscript Author Manuscript

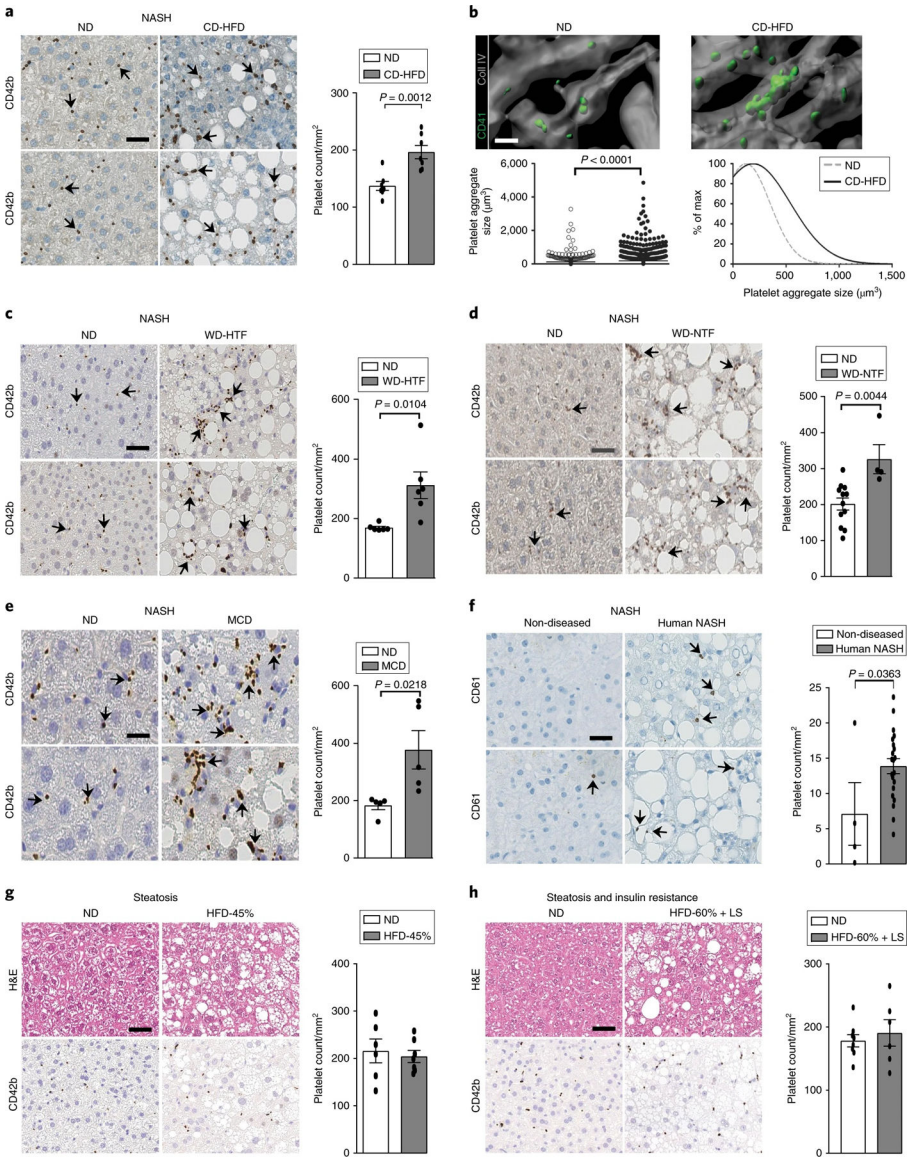

Fig. 1 |. Increased platelet numbers and aggregates in liver sinusoids of murine and human NASH.

a, CD42b staining and quantification of intrahepatic platelets ($CD42b^+$) in 6-month ND-fed or CD-HFD-fed mice; arrows indicate platelets ($n = 7$ mice/group). Scale bar, 50 μm. **b**, 3D confocal images of platelet (green)/liver endothelium (gray) interaction of 6-month ND-fed or CD-HFD-fed mice ($n = 4$ mice/group). Scale bar, 20 μm. **c**,**d**, CD42b staining and quantification in 6-month (**c**) ND-fed and WD-HTF-fed ($n = 6$ mice/group) or (**d**) WD-NTF-fed mice; arrows indicate platelets, (ND $n = 12$ mice; WD-HTF $n = 4$ mice). Scale bars, 50 μm. **e**, CD42b staining and quantification of intrahepatic platelets ($CD42b^+$) in 2-month ND-fed or MCD-fed mice; arrows indicate platelets ($n = 5$ mice/group). Scale bar, 50 μm. **f**, CD61 staining and quantification of platelets ($CD61^+$) in human livers; arrows indicate platelets (non-diseased patients $n = 4$; patients with NASH $n = 21$). **g**, H&E staining, CD42b staining and quantification in 6-month ND-fed or HFD-45%-fed mice (ND $n = 6$ mice; HFD-45% $n = 7$ mice). Scale bar, 50 μm. **h**, H&E, CD42b staining and quantification in

Author Manuscript Author Manuscript Author Manuscript Author Manuscript

6-month ND-fed or HFD-60%-fed (60% kcal and low sucrose (LS)) mice (ND $n = 8$ mice; HFD $n = 6$ mice). Scale bar, 50 μm. All data are shown as mean ± s.e.m. All data were analyzed using two-tailed Student's *t* test.

Author Manuscript Author Manuscript Author Manuscript Author Manuscript

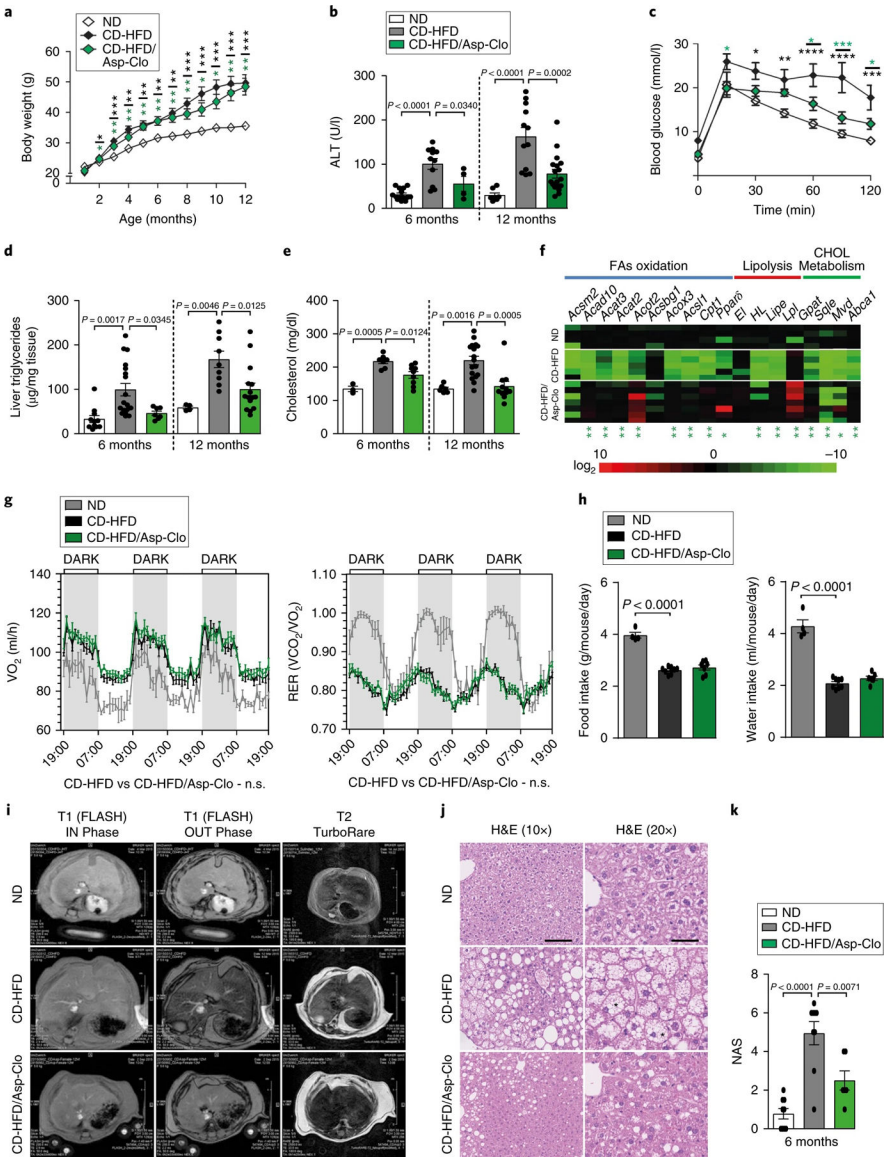

Fig. 2 |. Asp-Clo treatment results in attenuation of steatosis, liver damage, NASH and NASH-associated conditions.

a, Body weight development of 12-month ND-, CD-HFD- or CD-HFD/Asp-Clo-fed mice (ND $n = 5$ mice; CD-HFD $n = 5$ mice; CD-HFD/Asp-Clo $n = 9$). Statistic: ND vs CD-HFD (black asterisks), ND vs CD-HFD/Asp-Clo (green asterisks). **b**, ALT of 6- and 12-month ND-, CD-HFD or CD-HFD/Asp-Clo-fed mice (6 months: ND $n = 14$ mice; CD-HFD $n = 11$ mice; CD-HFD/Asp-Clo $n = 4$ mice; 12 months: ND $n = 7$ mice; CD-HFD $n = 12$ mice; CD-HFD/Asp-Clo $n = 18$ mice). **c**, Intraperitoneal glucose tolerance test (IPGTT) of 6-month ND-, CD-HFD- or CD-HFD/Asp-Clo-fed mice ($n = 5$ mice/group). Statistic: ND vs CD-HFD (black asterisks), ND vs CD-HFD/Asp-Clo (green asterisks). **d**,**e**, Liver triglyceride (6 months: ND $n = 11$ mice; CD-HFD $n = 15$ mice; CD-HFD/Asp-Clo $n = 7$ mice; 12 months: ND $n = 4$ mice; CD-HFD $n = 9$ mice; CD-HFD/Asp-Clo $n = 15$ mice) (**d**) and serum cholesterol (**e**) of 6- and 12-month ND-, CD-HFD- or CD-HFD/Asp-Clo-fed mice (6 months: ND $n = 4$ mice; CD-HFD $n = 7$ mice; CD-HFD/Asp-Clo $n = 9$ mice;

Author Manuscript Author Manuscript Author Manuscript Author Manuscript

12 months: ND $n = 6$ mice; CD-HFD $n = 17$ mice; CD-HFD/Asp-Clo $n = 11$ mice). **f**, Real-time qPCR analysis for genes involved in lipid metabolism/β-oxidation of 6-month ND-, CD-HFD- or CD-HFD/Asp-Clo-fed mice (ND $n = 4$ mice; CD-HFD $n = 5$ mice; CD-HFD/Asp-Clo $n = 7$ mice). Statistic: CD-HFD vs CD-HFD/Asp-Clo (green asterisks). **g**, Analysis of VO_2 and respiratory exchange ratio (RER) over time in 2-month ND-, CD-HFD- or CD-HFD/Asp-Clo-fed mice (ND $n = 4$ mice; CD-HFD $n = 8$ mice; CD-HFD/Asp-Clo $n = 8$ mice). **h**, Analysis of food (g/mouse/day) and water intake (ml/mouse/day) (ND $n = 4$ mice; CD-HFD $n = 8$ mice; CD-HFD/Asp-Clo $n = 6$ mice). **i**, MRI analyses in 6-month ND-, CD-HFD- or CD-HFD/Asp-Clo-fed mice ($n = 3$ mice/group). T1 (fast low-angle shot (FLASH)) OUT phase: dark color indicative of steatosis. T2 TurboRare: an increase in subcutaneous and abdominal fat and hepatic lipid accumulation (bright regions). **j**,**k**, H&E staining (**j**) and NAS evaluation (**k**) of 6-month ND-, CD-HFD- or CD-HFD/Asp-Clo-fed mice (ND $n = 9$ mice; CD-HFD $n = 9$ mice; CD-HFD/Asp-Clo $n = 6$ mice). Asterisks indicate damaged hepatocytes. Scale bars, 100 μm in 10×, 50 μm in 20×. All data are shown as mean ± s.e.m. Data in **a** and **c** were analyzed by two-way analysis of variance (ANOVA) with the post hoc Tukey's multiple comparison test; $*P < 0.05$.,$**P < 0.01$, $***P < 0.001$, $****P < 0.0001$. Data in **b**, **d**, **e**, **g**, **h** and **k** were analyzed by one-way analysis of variance with the post hoc Tukey's multiple comparison test. Data in **f** were analyzed by two-tailed Mann–Whitney test; $*P < 0.05$, $**P < 0.01$.

Author Manuscript Author Manuscript Author Manuscript Author Manuscript

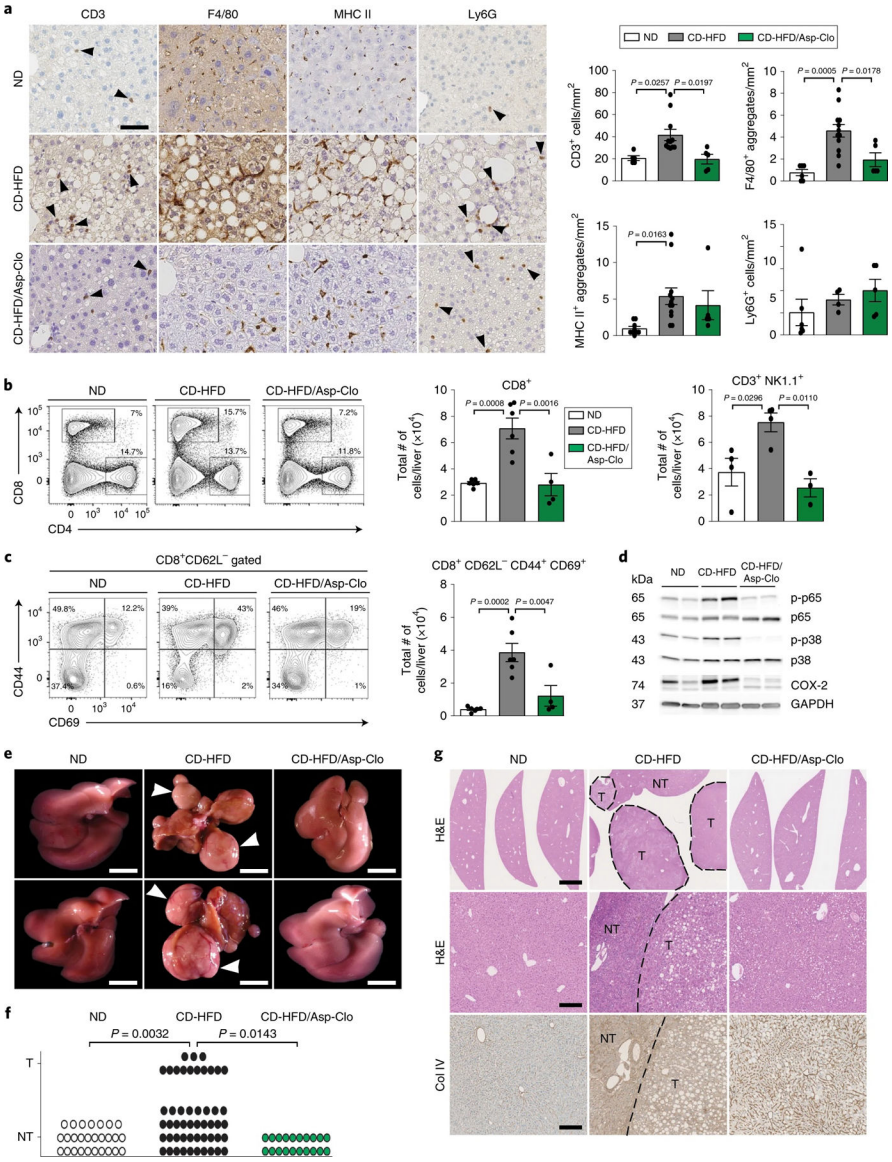

Fig. 3 |. Antiplatelet treatment with Asp-Clo abrogates immune cell infiltration into the liver and prevents NASH-induced HCC development.

a, CD3, F4/80, MHCII and Ly6G staining and quantification of 6-month ND-, CD-HFD- or CD-HFD/Asp-Clo-fed mice (CD3: ND $n = 5$ mice; CD-HFD $n = 11$ mice; CD-HFD/Asp-Clo $n = 5$ mice; F4/80: ND $n = 6$ mice; CD-HFD $n = 12$ mice; CD-HFD/Asp-Clo $n = 5$ mice; MHCII: ND $n = 9$ mice; CD-HFD $n = 12$ mice; CD-HFD/Asp-Clo $n = 5$ mice), scale bar, 50 μm. **b**,**c**, Representative FACS plots and quantification of hepatic CD4/CD8 ratio and NKT cells (**b**) and activated $CD8^+$ cells of 6-month ND-, CD-HFD- or CD-HFD/Asp-Clo-fed mice (**c**) ($CD8^+$: ND $n = 6$ mice; CD-HFD $n = 6$ mice; CD-HFD/Asp-Clo $n = 4$ mice; $CD3^+NK1.1^+$: ND $n = 4$ mice; CD-HFD $n = 4$ mice; CD-HFD/Asp-Clo $n = 3$ mice; $CD8^+CD62L–CD44^+CD69^+$: ND $n = 6$ mice; CD-HFD $n = 6$ mice; CD-HFD/Asp-Clo $n = 4$ mice). **d**, Western blot images of 6-month ND-, CD-HFD- or CD-HFD/Asp-Clo-fed mice ($n = 2$ mice/group). **e**, Representative macroscopical images of livers from 12-month ND-, CD-HFD- or CD-HFD/Asp-Clo-fed mice (ND $n = 0$ tumors in 27 mice; CD-HFD $n = 13$ tumors

Author Manuscript Author Manuscript Author Manuscript Author Manuscript

in 51 mice; CD-HFD/Asp-Clo $n = 0$ tumors in 20 mice). White arrowhead indicates HCC. Scale bar, 7.5 mm. **f**, HCC incidence of 12-month ND-, CD-HFD- or CD-HFD/Asp-Clo-fed mice. T, tumor; NT, non-tumor) (ND $n = 0$ tumors in 27 mice; CD-HFD $n = 13$ tumors in 52 mice; CD-HFD/Asp-Clo $n = 0$ tumors in 20 mice). **g**, HCC characterization by H&E and collagen IV (Col IV) staining of 12-month ND-, CD-HFD- or CD-HFD/Asp-Clo-fed mice; dashed line indicates tumor (T) border. Scale bar, 2 mm (top H&E) and 200 μm (middle H&E; bottom Col IV). All data are shown as mean ± s.e.m. Data in **a**–**c** were analyzed by one-way ANOVA with the post hoc Tukey's multiple comparison test. Data in **f** were analyzed using two-sided Fisher's exact test.

Author Manuscript Author Manuscript Author Manuscript Author Manuscript

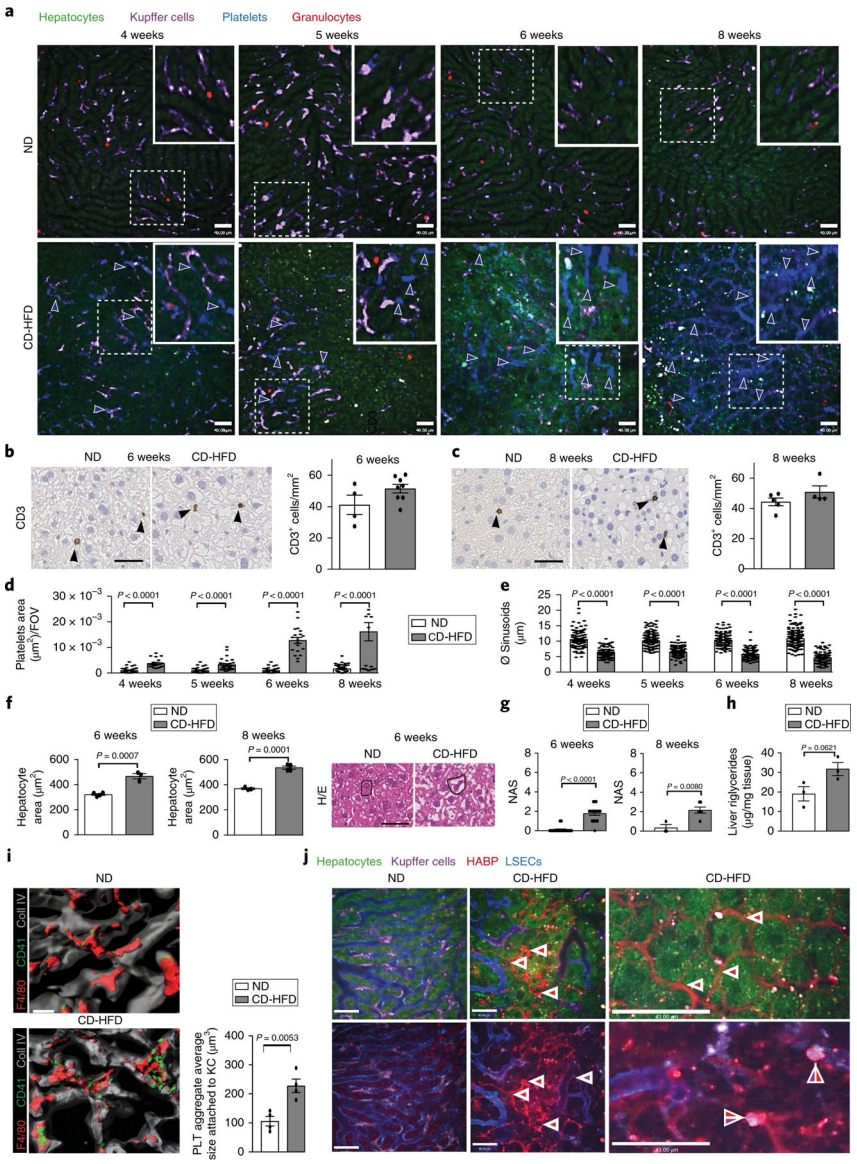

Fig. 4 |. Platelets efficiently populate the liver early during fatty liver pathogenesis.

a, Intravital microscopy of livers of 4, 5, 6 and 8 weeks ND- or CD-HFD-fed mice. Analysis of Kupffer cells (violet), platelets (blue) and granulocytes (red), (4 weeks: ND $n = 2$ mice; CD-HFD $n = 2$ mice; 5 weeks: ND $n = 2$ mice; CD-HFD $n = 2$ mice; 6 weeks: ND $n = 4$ mice; CD-HFD $n = 4$ mice; 8 weeks: ND $n = 3$ mice; CD-HFD $n = 3$ mice). Scale bars, 40 μm. **b**,**c**, CD3 staining and quantification of (**b**) 6-week (ND $n = 4$ mice; CD-HFD $n = 8$ mice) or (**c**) 8-week ND- or CD-HFD-fed mice (ND $n = 5$ mice; CD-HFD $n = 4$ mice). Scale bar, 50 μm. **d**, Quantification of platelet area by intravital microscopy of mice shown in **a** (ND: 4 weeks $n = 2$ mice and 40 FOV; 5 weeks $n = 2$ mice and 40 FOV; 6 weeks $n = 4$ mice and 40 FOV; 8 weeks $n = 2$ mice and 40 FOV; CD-HFD: 4 weeks $n = 2$ mice and 20 FOV; 5 weeks $n = 2$ mice and 20 FOV; 6 weeks $n = 4$ mice and 30 FOV; 8 weeks $n = 2$ mice and 19 FOV). **e**, Analysis of liver sinusoid diameter by intravital microscopy of mice shown in **a** (ND: 4 weeks $n = 2$ mice and 101 sinusoids; 5 weeks $n = 2$ mice and 150 sinusoids; 6 weeks

Author Manuscript Author Manuscript Author Manuscript Author Manuscript

n = 4 mice and 100 sinusoids; 8 weeks *n* = 2 mice and 150 sinusoids; CD-HFD: 4 weeks *n* = 2 mice and 100 sinusoids; 5 weeks *n* = 2 mice and 150 sinusoids; 6 weeks *n* = 4 mice and 100 sinusoids; 8 weeks *n* = 2 mice and 100 sinusoids). **f**, Hepatocyte swelling measurement by H&E of mice shown in **b** and **c** (6 weeks: ND *n* = 4 mice; CD-HFD *n* = 3 mice; 8 weeks: ND *n* = 3 mice; CD-HFD *n* = 4 mice). **g**, NAS evaluation of 6- or 8-week ND- or CD-HFD-fed mice (6 weeks: ND *n* = 19 mice; CD-HFD *n* = 18 mice; 8 weeks: ND *n* = 3 mice; CD-HFD *n* = 6 mice). **h**, Liver triglycerides of 6-week ND- or CD-HFD-fed mice (*n* = 3 mice/group). **i**, 3D confocal images and quantification of platelet (green)/Kupffer cells (red) interaction of 6-month ND- or CD-HFD-fed mice (*n* = 4 mice/group). Liver endothelium (gray). Scale bar, 20 μm. **j**, Left, representative images of intravital microscopy of 6-week ND- or CD-HFD-fed mice. Analysis of Kupffer cells (violet, violet arrowhead), hyaluronan binding protein (HABP) (red, red arrowhead) and LSECs (blue). Scale bar, 43 μm. Right, representative high-magnification images of intravital microscopy of mice shown in **i**, analysis of Kupffer cells (violet, violet arrowhead), HABP (red, red arrowhead) and LSECs (blue), (ND *n* = 4 mice; CD-HFD *n* = 4 mice). Scale bar, 43 μm. All data are shown as mean ± s.e.m. All data were analyzed using two-tailed Student's *t* test.

Author Manuscript Author Manuscript Author Manuscript Author Manuscript

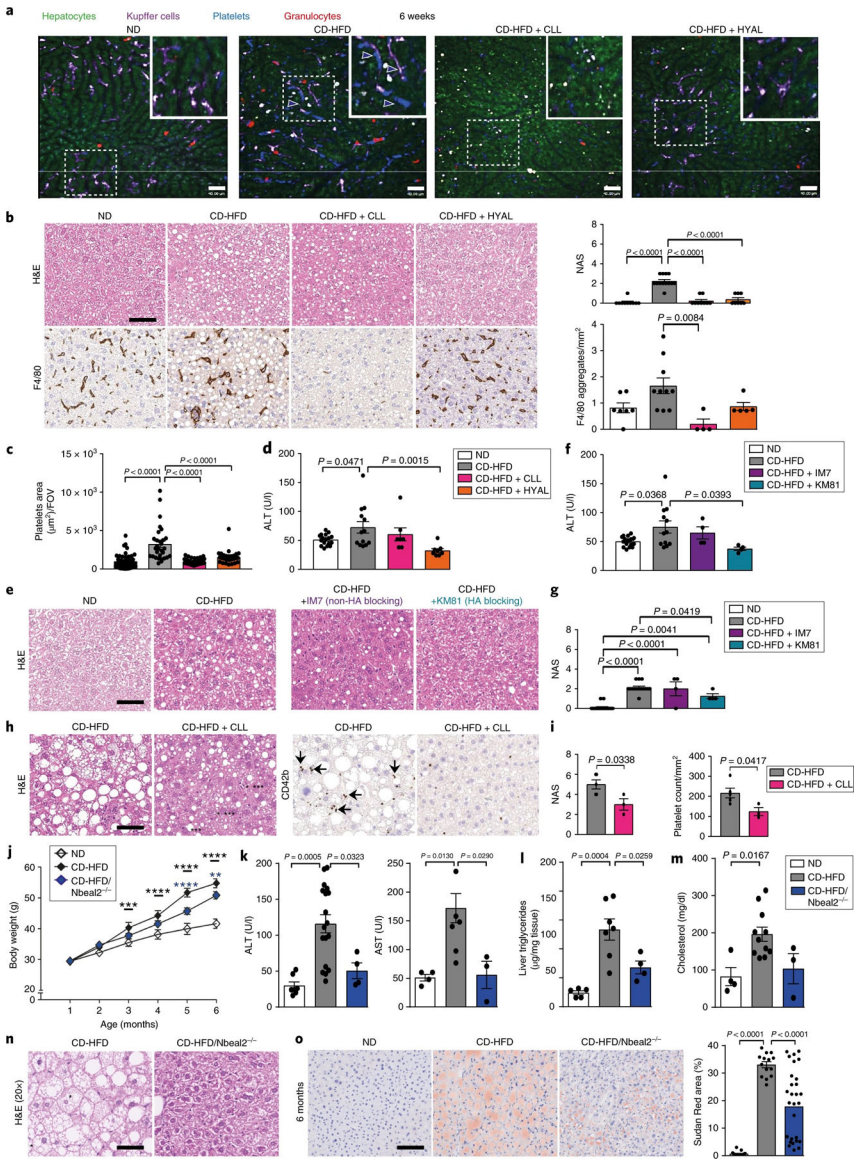

Fig. 5 |. Intrahepatic platelet accumulation depends on Kupffer cells, hyaluronan and cargo function.

a, Representative images of intravital microscopy after treatment (clodronate liposomes (CLL) or hyaluronidase (HYAL)) in 6-week ND-, CD-HFD-, CD-HFD + CLL- or CD-HFD + HYAL-fed mice. Analysis of Kupffer cells (violet), platelets (blue, blue arrowhead), and granulocytes (red), (n = 4 mice/group). Scale bar, 40 μm. **b**, H&E and F4/80 staining with quantification and NAS evaluation after treatment in 6-week ND-, CD-HFD-, CD-HFD + CLL- or CD-HFD + HYAL-fed mice (H&E: ND n = 10 mice; CD-HFD n = 14 mice; CD-HFD + CLL n = 9 mice; CD-HFD + HYAL n = 8 mice; F4/80: ND n = 7 mice; CD-HFD n = 10 mice; CD-HFD + CLL n = 4 mice; CD-HFD + HYAL n = 5 mice). Scale bar: 50 μm. **c**, Quantification of platelet area by intravital microscopy of mice shown in **a** (ND n = 4 mice and 40 FOV; CD-HFD n = 4 mice and 30 FOV; CD-HFD + CLL n = 4 mice and 40 FOV; CD-HFD + HYAL n = 4 mice and 30 FOV). **d**, ALT levels of mice shown in **b** (ND n = 17 mice; CD-HFD n = 13; CD-HFD + CLL n = 7 mice; CD-HFD

Author Manuscript Author Manuscript Author Manuscript Author Manuscript

+ HYAL $n = 8$ mice). **e**–**g**, H&E histology (**e**), ALT levels (**f**) and NAS evaluation (**g**) after anti-CD44 antibody treatment (anti-CD44 antibody blocking (KM81) or non-blocking (IM7) HA-binding site) in 6-week ND-, CD-HFD-, CD-HFD + IM7 (non-HA blocking)-or CD-HFD + KM81 (HA-blocking)-fed mice (ALT: ND $n = 16$ mice; CD-HFD $n = 12$ mice; CD-HFD + IM7 $n = 4$ mice; CD-HFD + KM81 $n = 4$ mice; H&E and NAS: ND $n = 19$ mice; CD-HFD $n = 15$ mice; CD-HFD + IM7 $n = 4$ mice; CD-HFD + KM81 $n = 4$ mice). Scale bars, 50 μm. **h**,**i**, Representative H&E and CD42b staining (**h**) and NAS evaluation and platelet quantification (**i**) after CLL treatment in 6-month CD-HFD -or CD-HFD + CLL-fed mice (H&E and NAS: CD42b: CD-HFD $n = 5$ mice; CD-HFD + CLL $n = 3$ mice; CD42b: CD-HFD $n = 5$ mice; CD-HFD + CLL $n = 3$). **j**, Body weight development of 6-month ND-fed, CD-HFD-fed or CD-HFD/Nbeal2$^{-/-}$ mice (ND $n = 6$ mice; CD-HFD $n = 6$ mice; CD-HFD/Nbeal2$^{-/-}$ $n = 4$ mice). Statistic: ND vs CD-HFD (black asterisks), CD-HFD vs CD-HFD/Nbeal2$^{-/-}$ (blue asterisks). **k**–**m**, ALT, AST levels (**k**) liver triglycerides (**l**) and serum cholesterol (**m**) of mice shown in **i** (ALT: ND $n = 7$ mice; CD-HFD $n = 18$ mice; CD-HFD/Nbeal2$^{-/-}$ $n = 4$ mice; AST: ND $n = 4$ mice; CD-HFD $n = 8$ mice; CD-HFD/Nbeal2$^{-/-}$ $n = 3$ mice; liver triglycerides: ND $n = 5$ mice; CD-HFD $n = 7$ mice; CD-HFD/Nbeal2$^{-/-}$ $n = 4$ mice; serum cholesterol: ND $n = 4$ mice; CD-HFD $n = 11$ mice; CD-HFD/Nbeal2$^{-/-}$ $n = 3$ mice;). **n**, Representative H&E of mice shown in **i** (CD-HFD n = 9 mice; CD-HFD/Nbeal2$^{-/-}$ $n = 10$ mice), damaged hepatocytes (asterisks) are indicated. Scale bar, 50 μm. **o**, Fat quantification by Sudan red staining of mice shown in **i** (ND $n = 4$ mice and 17 fields; CD-HFD $n = 4$ mice and 14 fields; CD-HFD/Nbeal2$^{-/-}$ $n = 4$ mice and 35 fields). Scale bar, 100 μm. All data are shown as mean ± s.e.m. Data in **b**–**d**,**f**,**g**,**k**–**m**,**o** were analyzed by one-way ANOVA with the post hoc Tukey's multiple comparison test. Data in **i** were analyzed using two-tailed Student's *t* test. Data in **j** were analyzed using two-way analysis of variance with the post hoc Tukey's multiple comparison test. *$P < 0.05$, **$P < 0.01$, ***$P < 0.001$, ****$P < 0.0001$.

Author Manuscript Author Manuscript Author Manuscript Author Manuscript

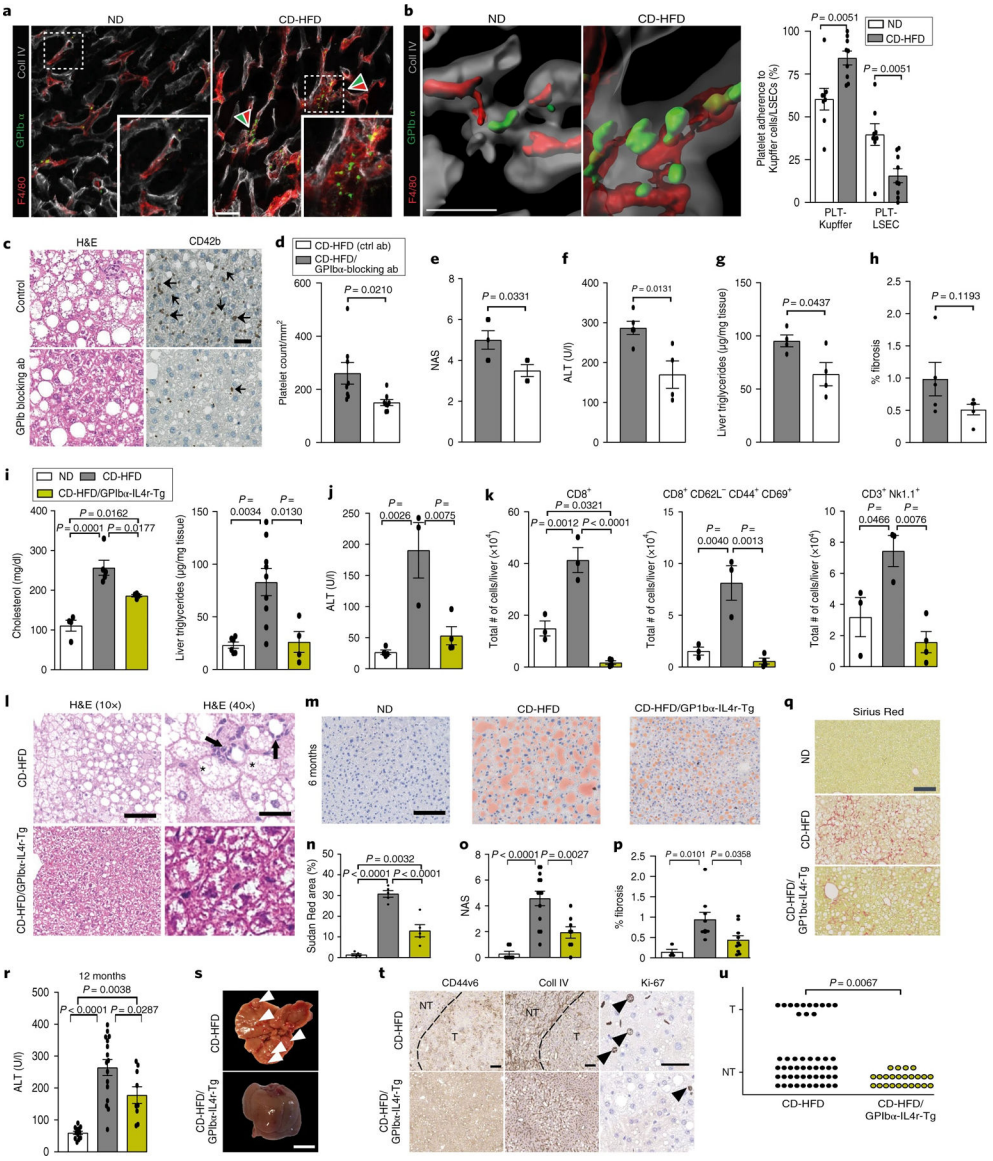

Fig. 6 |. Anti-GPIbα antibody treatment as well as genetic dysfunction of GPIbα reduces NASH, fibrosis and HCC development.

a, Representative 3D confocal images of GPIbα (green, green arrowheads) and Kupffer cells (red, red arrowheads) interaction of 6-month ND- or CD-HFD-fed mice (ND $n = 4$ mice; CD-HFD $n = 4$ mice). Liver endothelium (gray), scale bar, 30 μm. **b**, High-magnification 3D confocal images and quantification of GPIbα (green)/Kupffer cells (red) and GPIbα (green)/LSECs (gray) interaction in 6-month ND- or CD-HFD-fed mice (ND $n = 4$ mice and 2 FOV/mouse; CD-HFD $n = 4$ mice and 2 FOV/mouse) Scale bar, 3 μm. For visualization of intravascular events, the transparency of the sinusoidal rendering was set to 50%. **c**, Representative H&E and CD42b staining after 5 weeks of GPIbα blocking or control Fab in 6-month CD-HFD-fed mice; scale bar, 50 μm. Platelets are indicated by arrows. **d**–**h**, Platelet quantification (**d**), NAS evaluation (**e**), ALT levels (**f**), liver triglycerides (**g**) and quantification of Sirius red–positive areas (**h**) of mice shown in **c** (CD42b staining and platelet quantification: CD-HFD + control Fab $n = 8$ mice; CD-HFD + GPIbα blocking

Author Manuscript Author Manuscript Author Manuscript Author Manuscript

Fab n = 8 mice; H&E, NAS and ALT: CD-HFD + control Fab n = 5 mice; CD-HFD + GPIbα blocking Fab n = 4 mice; liver triglycerides: CD-HFD + control Fab n = 4 mice; CD-HFD + GPIbα blocking Fab n = 4 mice; Fibrosis: CD-HFD + control Fab n = 5 mice; CD-HFD + GPIbα blocking Fab n = 4 mice). **i**,**j**, Serum cholesterol, liver triglycerides (**i**) and ALT levels (**j**) of 6-month ND, CD-HFD- or CD-HFD/*hIL4rα/GPIbα*-Tg mice (serum cholesterol: ND n = 4 mice; CD-HFD n = 5 mice; CD-HFD/*hIL4rα/GPIbα*-Tg n = 4 mice; liver triglycerides: ND n = 6 mice; CD-HFD n = 5 mice; CD-HFD/*hIL4rα/GPIbα*-Tg n = 4 mice; ALT: ND n = 4 mice; CD-HFD n = 3 mice; CD-HFD/*hIL4rα/GPIbα*-Tg n = 4 mice). **k**, Quantification by flow cytometry of intrahepatic immune cells (CD8 + T cells (left), activated CD8+ T cells (middle), NKT cells (right)) of mice shown in **i** (CD8+, activated CD8+ and NKT cells: ND n = 3 mice; CD-HFD n = 3 mice; CD-HFD/*hIL4rα/GPIbα*-Tg n = 4 mice). **l**, Representative H&E staining of mice shown in **i**, indications of damaged hepatocytes (asterisks) and satellitosis (arrows); scale bars, 100 μm in 10× and 25 μm in 40×. m–o, Sudan red staining (**m**) and quantification of Sudan red–positive areas (**n**), NAS evaluation (**o**) of 6-month ND, CD-HFD or CD-HFD/*hIL4rα/GPIbα*-Tg mice (H&E and NAS: ND n = 7 mice; CD-HFD n = 13 mice; CD-HFD/*hIL4rα/GPIbα*-Tg n = 8 mice; Sudan red staining and quantification: n = 5 mice/group). **p**,**q**, Fibrosis quantification (**p**) and Sirius red staining (**q**) of 12-month ND, CD-HFD or CD-HFD/*hIL4rα/GPIbα*-Tg mice (H&E and NAS: ND n = 7 mice; CD-HFD n = 13 mice; CD-HFD/*hIL4rα/GPIbα*-Tg n = 8 mice; Sudan red: n = 5 mice/group; fibrosis and Sirius red: ND n = 4 mice; CD-HFD n = 9 mice; CD-HFD/*hIL4rα/GPIbα*-Tg n = 10 mice). **r**, ALT levels of 12-month ND, CD-HFD or CD-HFD/*hIL4rα/GPIbα*-Tg mice (ND n = 12 mice; CD-HFD n = 16 mice; CD-HFD/*hIL4rα/GPIbα*-Tg n = 9 mice). **s**, Macroscopical images of tumors of mice shown in **r**; tumor nodules are indicated by arrowhead) (CD-HFD: n = 13 tumors in 52 mice; CD-HFD/*hIL4rα/GPIbα*-Tg: n = 0 tumors in 24 mice); scale bar, 750 μm. **t**, HCC characterization by CD44v6, Collagen IV (Coll IV) and Ki67 staining form mice shown in **r**. Arrowheads indicate positive hepatocytes, dashed line indicates tumor (T) border; scale bar, 200 μm (CD44v6 and Coll IV), 50 μm (Ki67). **u**, HCC incidence (T = HCC; NT = non-tumor) from 12-month CD-HFD-fed or CD-HFD/*hIL4rα/GPIbα*-Tg mice, CD-HFD: n = 13 tumors in 52 mice; CD-HFD/*hIL4rα/GPIbα*-Tg: n = 0 tumors in 24 mice). All data are shown as mean ± s.e.m. Data in **b**,**d**–**h** were analyzed by two-tailed Student's t test. Data in **i**–**k**,**n**–**p**,**r** were analyzed by one-way ANOVA with the post hoc Tukey's multiple comparison test. Data in **u** were analyzed by two-sided Fisher's exact test.